Ocean Engineering 286 (2023) 115709

Contents lists available at ScienceDirect

Ocean Engineering

journal homepage: www.elsevier.com/locate/oceaneng

Coupled responses of the flow-induced vibration and flow-induced rotation of a rigid cylinder-plate body

Tao Tang [a,b], Hongjun Zhu [a,*], Qing Xiao [b,**], Quanyu Chen [a], Jiawen Zhong [a], Yingmei Li [a], Tongming Zhou [c]

[a] State Key Laboratory of Oil and Gas Reservoir Geology and Exploitation, Southwest Petroleum University, Chengdu, 610500, China
[b] Department of Naval Architecture, Ocean and Marine Engineering, University of Strathclyde, Glasgow, G4 0LZ, United Kingdom
[c] Department of Civil, Environmental and Mining Engineering, The University of Western Australia, Crawley, WA 6009, Australia

ARTICLE INFO

Handling Editor: Prof. A.I. Incecik

ABSTRACT

In this study, coupled responses of flow-induced vibration and rotation for an elastically mounted cylinder-plate body are numerically investigated at a low Reynolds number of 120. A wide vibrational reduced velocity range of $U_y = 3$–18 under four rotational reduced velocities $U_\theta = 5$, 8, 12, and 18 are considered. The non-bifurcation responses, bifurcation only in rotation responses, and bifurcation in both vibration and rotation responses are identified. Typical vortex-induced vibration (VIV) responses are recognized when considering the passive rotations, different from the full interactions between VIV and galloping for the vibration-only case. As U_θ increases, the peak vibration amplitudes increase, the onset U_y of the lock-in region becomes larger, and the lock-in region is wider. The phase angles of displacements versus lift coefficients experience a jump from 0° to 180° in the lock-in region, and the larger the U_θ, the wider the U_y range of phase jump. Whether the instantaneous posture of the cylinder-plate body is streamlined or not is determined by oscillation amplitudes and phase differences between displacements versus rotation angles. Streamlined profiles can be achieved under small oscillation amplitudes or when the phase angles are nearly 90°. The 2S (two isolated vortices) vortex shedding mode dominates the initial and desynchronization branch, while the 2P (two pairs of vortices), 2S* (two isolated vortices with tendency to split), and 2T (two triplets of vortices) modes appear in the lock-in region. After the symmetry-breaking bifurcation, the reattachment behavior becomes simpler and the length of the recirculation region is significantly increased, as compared with those in non-bifurcation region. With the above study, a new method of improving energy harvesting from flow-induced vibration, by incorporating passive rotations simultaneously, is first introduced. It is found that passive rotations can enhance the vibration responses and thus lead to the increased output power and energy transfer ratio, although they make less contributions to the total power. Generally, this mechanical system presents a promising opportunity for energy harvesting through flow-induced vibration.

1. Introduction

The flow dynamics around bluff bodies, particularly circular cylinders, have received much attention due to their wide-ranging applications in various engineering fields such as offshore risers, heat exchangers, bridges and buildings. When the Reynolds number Re (= UD/υ, where U is the free stream velocity, D is the diameter of a circular cylinder, and υ is the fluid kinematic viscosity) exceeds 47 (Henderson, 1997), the flow boundary layers separated from the cylinder surface can generate alternating vortices. These alternating-shedding vortices can generate fluctuating hydrodynamic forces on the structure, resulting in dynamic responses that are often undesirable in engineering applications. Consequently, numerous methods have been proposed and developed to suppress vortex shedding. In general, there are two categories of control strategies: active and passive methods. Power input is required for the former (Zhu et al., 2019, 2020b; Huang et al., 2017), while the later can be easily achieved by modifying the structural cross-sections or attaching additional devices without external power sources (Choi et al., 2008; Zdravkovich, 1981; Rashidi et al., 2016). As a result, passive control methods have gained increasing attention in

* Corresponding author.
** Corresponding author.
E-mail addresses: zhuhj@swpu.edu.cn (H. Zhu), qing.xiao@strath.ac.uk (Q. Xiao).

https://doi.org/10.1016/j.oceaneng.2023.115709
Received 12 June 2023; Received in revised form 9 August 2023; Accepted 23 August 2023

recent decades. A typical passive device used for regulating and stabilizing wake flows is the splitter plate, which is usually attached to the rear base of a circular cylinder, forming a cylinder-plate body. A large number of reports (Apelt et al., 1973; Apelt and West, 1975; Kwon and Choi, 1996; Hwang et al., 2003; Serson et al., 2014; Ozone, 1999; Qiu et al., 2014; Ozkan et al., 2017) have demonstrated that the drag force on a stationary cylinder-plate body can be significantly reduced by recovering the base pressure in the near wake. Meanwhile, the vortex shedding is also suppressed by the splitter plate.

1.1. Flow-induced vibration of a cylinder-plate body

When fluid flows over elastically-mounted bluff bodies, two distinct flow-induced vibration (FIV) responses commonly arise: vortex-induced vibration (VIV) and galloping. In the case of VIV response under laminar flows, the vibration frequency firstly increases with the flow velocity in the initial branch (IB) when the cylinder starts vibrating. The well-known "lock-in" phenomenon is observed when the vibration frequency closely matches the structural natural frequency, leading to relatively large amplitudes. However, as the flow velocity further increases, the vibration response sequentially transitions into the lower branch (LB) and desynchronization branch (DB). In these regions, the amplitudes gradually decrease and eventually approach nearly zero, while the frequencies follow the Strouhal number. Consequently, the VIV exhibits self-excited nonlinear motion with limited vibration amplitudes. In contrast, galloping manifests as a fluid instability phenomenon with larger or even uncontrollable amplitudes. This aero- or hydro-elastic instability is typically attributed to the reattachment behavior of shear layers (Zhu et al., 2020a) for the structures with a non-circular cross section. It is sustained by the asymmetric long-time dynamic force arising from the body motion in fluid. Structures undergoing galloping exhibit high amplitudes and low frequencies (Tang et al., 2023a). Additionally, there are instances where galloping and VIV interact with each other (Mannini et al., 2014, 2016).

A splitter plate is expected to delay the interaction of shear layers and therefore reduce the hydrodynamic forces, consequently mitigating the flow-induced vibration (FIV) responses of a circular cylinder. However, this approach often fails to achieve its goal. A lot of scholars (Kawai, 1990; Zhu et al., 2020a; Hu et al., 2021; Sahu et al., 2019; Assi et al., 2009; Assi and Bearman, 2015; Stappenbelt, 2010; Liang et al., 2018; Sun et al., 2020, 2022; Song et al., 2017) suggested that, instead of the vortex-induced vibration observed in the case of a bare cylinder, galloping-type oscillations are typically found for a cylinder-plate body. Some noteworthy examples are as follows. The work of Assi et al. (2009) reported galloping responses of a circular cylinder equipped with a (0.25–2)D rigid splitter plate. Later, Assi and Bearman (2015) experimentally demonstrated that the reattachment of shear layers to the tip of splitter plates serves as the hydrodynamic mechanism of galloping responses. This finding is further identified by Zhu et al. (2020a), and they suggested that the longer the plate, the larger the onset reduced velocity of galloping. Sun et al. (2022) observed pronounced galloping responses of a cylinder-plate body at $L^* = 0.4$–3.2 ($L^* = L/D$, L is the plate length), and attributed to the low-pressure region near the splitter plate as a favorable trigger for galloping. Stappenbelt (2010) conducted experiments in a water tunnel to study the vibration responses of a cylinder-plate body. Results showed that the galloping-type response halts abruptly at high reduced velocity ranges when $L^* < 0.5$. In the range of $0.5 < L^* < 2.8$, no-limited galloping response is presented. Further lengthening plate, no significant VIV or galloping is observed. Liang et al. (2018) studied FIV responses of a cylinder-plate body and identified four distinct types: (1) VIV-only at $L^* = 0.4$, 0.5; (2) full interaction between VIV and galloping at $L^* = 1.0$, 1.5; (3) a VIV regime and partial interaction between VIV and galloping at $L^* = 2.0$, 2.5, 3.5; and (4) VIV regime and classical galloping at $L^* = 4.5$, 5.0. Regarding the transition mechanism from VIV to galloping, Sun et al. (2020) found that the lift components generated from the splitter plate and the circular cylinder behave, respectively, as driving and suppressing forces of galloping. The transition from VIV to galloping can thus be understood as the result of the competition between these two forces.

1.2. Flow-induced rotation of a cylinder-plate body

In addition to the flow-induced vibration, the cylinder-plate body may trigger flow-induced rotation (FIR) responses due to the flow-induced torsional moment. Xu et al. (1990) conducted the first investigation on the flow characteristics over a freely-rotating cylinder-plate body at $L^* = 1$ within a low Reynolds number range of 1–50. A critical Reynolds number, $\mathrm{Re_c} = 28$, was identified in their work. Below $\mathrm{Re_c}$, the flow exhibits symmetry with a stable equilibrium position of $\overline{\theta} = 0$, where $\overline{\theta}$ is the time-averaged rotation angle. However, at $\mathrm{Re} = \mathrm{Re_c}$, the cylinder-plate body starts to migrate to a non-zero offset angle, which is well known as the symmetry-breaking bifurcation phenomenon. Later, Xu et al. (1993) confirmed that the different separated flows on the two sides of the splitter plate destabilize the symmetric equilibrium position and thus the bifurcation. The length of the splitter plate plays a significant role in the occurrence of bifurcation phenomenon. In general, the longer the plate, the smaller the $\overline{\theta}$, i.e., the bifurcation is less likely to occur for a circular cylinder attached with a long splitter plate (Cimbala and Garg, 1991; Cimbala and Chen, 1994; Assi et al., 2009; Gu et al., 2012; Tang et al., 2022b). Taking into account the rotational stiffness and damping, Lu et al. (2016) found that the critical reduced velocity corresponding to the onset of bifurcation is lower for circular cylinders with longer splitter plates. Zhang et al. (2021) suggested that reducing the moment of inertia of an elastically-mounted cylinder-plate body leads to a decrease in the critical reduced velocity for bifurcation. In addition to the attached cases, Zhu et al. (2022) investigated the free-rotating responses of a circular cylinder fitted with a detached splitter plate. Their results illustrated the existence of bifurcation within the range of $0 \le G^* \le 0.5$ while its disappearance at $0.55 \le G^* \le 2$, where $G^* = G/D$ and G is the gap distance between the cylinder and plate. For an elastically mounted cylinder-plate body, Tang et al. (2022a) showed that the critical reduced velocity associated with the appearance of bifurcation increases as G^* increases.

1.3. Coupled responses of a cylinder-plate body

Compared with the considerable reports focusing on individual flow-induced vibration or rotation responses of a cylinder-plate body, investigations into the coupled analysis of vibration and rotation are relatively scarce. Experimental results by Assi et al. (2009) showed that the vortex-induced vibration of a circular cylinder can be practically eliminated by using free-to-rotate splitter plates. The largest drag reduction is equal to about 60% of that of a stationary bare cylinder. Later on, Assi et al. (2014) emphasized the significant influence of torsional friction on FIV responses. Specifically, they observed that when the cylinder-plate body undergoes rotation, enhanced vibration responses occur under low torsional friction ($\tau_f = 0.009$Nm/m). In contrast, when relatively large torsional friction ($\tau_f = 0.035$Nm/m) is considered, the transverse vibration amplitudes of the rotatable cylinder-plate body are hugely reduced.

1.4. Background and novelty of this work

To the authors' knowledge, most of previous studies on a cylinder-plate body considered a single-degree-of-freedom vibration/rotation in the transverse/torsional direction, or considered a two-degree-of-freedom vibration in the in-flow and transverse direction. By comparison, the understanding of the coupled responses of flow-induced vibration and rotation of a cylinder-plate body is lacking. Only several experimental investigations are conducted as reviewed in Sec. 1.3, and there remains a lack of flow details and discussion about the interactions

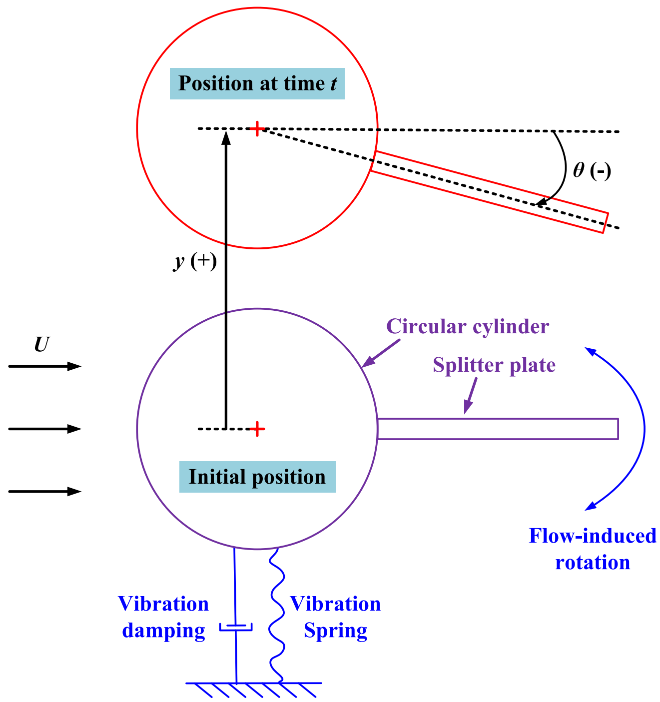

Fig. 1. Schematic of the cylinder-plate body at initial position and the position at a given time *t*.

between vibration and rotation. In fact, the flow-induced vibration and flow-induced rotation are usually coexisting in nature and engineering applications, typically exemplified by the fluttering motion of leaves and the offshore wind turbine. Therefore, some open questions need to be explained. Could the vibration soften rotation responses or not? How does the rotation influence vibration responses? To address these open questions as far as possible, this study focuses on investigating the coupled responses of a cylinder-plate body, and it is expected to gain insight into the inherent relationship between flow-induced vibration and rotation.

Another topic we are concerned about is the potential utilization of energy harvesting from coupled responses of flow-induced vibration and rotation for the cylinder-plate body. Due to the worldwide increasing energy demand, the request to explore new approaches to harvest clean, renewable, and economical energy is arising. Ever since Bernitsas et al. (2008) proposed the concept of the Vortex-Induced Vibration Aquatic Clean Energy (VIVACE), energy harvesting from flow-induced vibrations has been rapidly developed (Rostami and Armandei, 2017; Wang et al., 2020). This mechanical energy contained in vibrating oscillators is considered as a good energy source because it possesses a considerable power density and less influenced by weather as compared to solar-, wave-, and wind-energy harvesters. Accordingly, a large number of scholars have conducted experimental and numerical investigations to improve the ability of energy harvesting from flow-induced vibrations. Typical methods includes alteration of cross-sections of bluff body, utilization of wake flow and interference, modification and rearrangement of cantilever beams, and introduction of magnetic force, as Zhu et al. (2021b) suggested. In this work, we employ a markedly distinct approach by incorporating passive rotations simultaneously to study the energy harvesting ability from flow-induced vibration. This innovative method is first proposed, and we try to ascertain the extent to which passive rotations can augment vibration responses and improve the energy harvesting.

1.5. Objective and remainder of this work

Based on the literature review and analyses in Sec. 1.4, it is believed that the relevant work on the coupled responses of flow-induced vibration and flow-induced rotation of an elastically-mounted cylinder-plate body is rare. The interactions between vibrations and rotations and the associated underlaying flow mechanism need to be further illustrated for the purpose of better understanding on this fundamental physical phenomenon and thus providing some useful practical guidances. Therefore, with the help of ANSYS-FLUENT, this work presents numerical simulations to investigate the coupled responses of flow-induced vibration and flow-induced rotation of a cylinder-plate body which is formed by a circular cylinder and a splitter plate attaching to the cylinder. This investigation is conducted at a fixed low Reynolds number of 120 for a wide vibrational reduced velocity range of 3–18 and four rotational reduced velocities of 5, 8, 12, and 18. The following four main aspects are thoroughly examined and discussed: (1) coupled responses of flow-induced vibration and rotation of the cylinder-plate body; (2) relationships between structural motions (especially the instantaneous structural postures) and phase differences (displacement v.s. lift and displacement v.s. rotation angle); (3) valuable insights into the flow characteristics and wake patterns; and (4) the potential application for energy harvesting from this system. To achieve the above main objectives, the reminder of this paper is organized as follows. Section 2 outlines the configuration of the cylinder-plate body, presents the governing equations of fluid-structure interaction system, describes the computational mesh, and validates the employed numerical method. Section 3 presents and discusses the numerical results. Finally, the major conclusions are drawn in Section 4.

2. Mathematical method

2.1. Model configuration

Fig. 1 illustrates the configuration employed in this study, where a rigid splitter plate is attached to the rear of a circular cylinder, forming a unified cylinder-plate body. The diameter of the circular cylinder, length and thickness of the splitter plate are set to D, D, and $0.1D$, respectively. The cylinder-plate body is subjected to a uniform cross flow and allowed to passively vibrate and rotate in the transverse and torsional directions, respectively. The present fluid-structure interactions are treated as a coupled dynamic system by fully considering the vibration/rotation stiffness and damping. As the fluid-structure interaction takes place, the cylinder-plate body initiates vibration/rotation responses and moves to a new position (y, θ) at a given time t, where y (positive when moving upwards) and θ (negative when rotating clockwise) are the transverse displacement and rotational angle, respectively.

2.2. Governing equations and numerical solutions

For the problem of an elastically mounted cylinder-plate body in a uniform laminar flow, the two-dimensional fluid flows can be described by the incompressible Navier-Stokes equations including the continuity and momentum equations. The non-dimensional forms are written as (Bhatt and Alam, 2018):

$$\nabla \cdot \boldsymbol{u}^* = 0 \tag{1}$$

$$\frac{\partial \boldsymbol{u}^*}{\partial t^*} + (\boldsymbol{u}^* \cdot \nabla)\boldsymbol{u}^* = -\nabla p^* + \frac{1}{\mathrm{Re}}\nabla^2 \boldsymbol{u}^* \tag{2}$$

where $\boldsymbol{u}^*$ is the normalized flow velocity vector in the Cartesian coordinate system with its two components of u^* ($= u/U$) in the in-line direction and v^* ($= v/U$) in the cross-flow direction, t^* ($= tU/D$) the non-dimensional flow time, t the flow time, p^* ($= p/\rho U^2$) the dimensionless pressure, p the pressure and ρ the fluid density.

The governing structural equation for transverse vibrations can be expressed by using the classical mass-spring-damping system (Zhu et al., 2018):

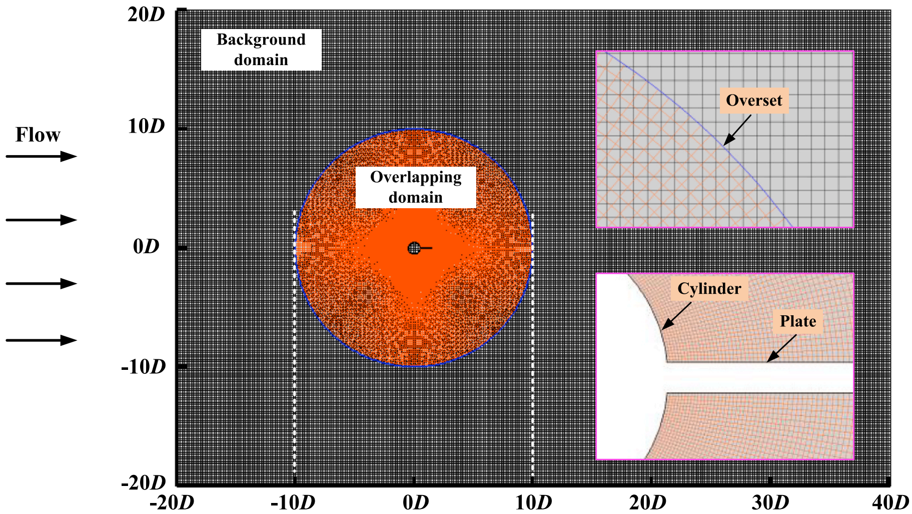

Fig. 2. Computational domain and mesh system.

Table 1
Convergence analysis on overlapping domains, where the coupled responses of the cylinder-plate body at $U_y = 8$ and $U_\theta = 8$ are compared.

Diameter of the concentric circle	$\overline{Y}$	Y_A	$\overline{\theta}$	θ_A
18*D*	0.00668	0.78826	0.00659	0.69363
20*D*	0.00679 (1.65%)	0.81199 (3.01%)	0.00672 (1.97%)	0.71209 (2.66%)
22*D*	0.00681 (0.29%)	0.81451 (0.31%)	0.00673 (0.15%)	0.71836 (0.88%)

$$m\ddot{y} + C_y\dot{y} + K_y y = F_L \tag{3}$$

where m is the structural mass, y, $\dot{y}$, and $\ddot{y}$ the displacement, velocity, and acceleration, respectively, C_y the vibrational damping constant which is a lumped parameter including the viscous damping, dry friction damping, fluid damping, or added damping, K_y the vibrational stiffness constant that provides the restoring forces generated by the spring elements of the system, and F_L the lift force. The non-dimensional form of Eq. (3) is:

$$\ddot{Y} + 2\zeta_y\left(\frac{2\pi}{U_y}\right)\dot{Y} + \left(\frac{2\pi}{U_y}\right)^2 Y = \frac{C_L}{2m^*} \tag{4}$$

where

$$Y = \frac{y}{D}\ (\text{non}-\text{dimensional displacement}) \tag{5}$$

$$\zeta_y = \frac{C_y}{2\sqrt{K_y m}}\ (\text{vibrational damping ratio}) \tag{6}$$

$$U_y = \frac{U}{f_{ny}D}\ (\text{vibrational reduced velocity}) \tag{7}$$

$$f_{ny} = \frac{1}{2\pi}\sqrt{\frac{K_y}{m}}\ (\text{vibrational natural frequency, changed with } U_y) \tag{8}$$

$$m^* = \frac{m}{m_d}\ (\text{mass ratio, and } m_d \text{ is the displaced fluid mass}) \tag{9}$$

$$C_L = \frac{2F_L}{\rho U D^2}\ (\text{lift coefficient}) \tag{10}$$

For the one-degree-of-freedom rotational mode, the governing equation is governed by the (mass moment of inertia)-spring-damping system (Tang et al., 2022a; Robertson et al., 2003):

$$I_\theta\ddot{\theta} + C_\theta\dot{\theta} + K_\theta\theta = M_\theta \tag{11}$$

where I_θ is the mass moment of inertia, C_θ the rotational damping constant, K_θ the rotational stiffness constant, M_θ the moment with respect to the cylinder center, θ (unit: radian) the rotational angle of the body around the elastic centre, $\dot{\theta}$ the angular velocity, and $\ddot{\theta}$ the angular acceleration. The non-dimensional form of Eq. (11) is:

$$\ddot{\theta} + 2\zeta_\theta\left(\frac{2\pi}{U_\theta}\right)\dot{\theta} + \left(\frac{2\pi}{U_\theta}\right)^2 \theta = \frac{C_M}{2I_\theta^*} \tag{12}$$

where

$$\zeta_\theta = \frac{C_\theta}{2\sqrt{K_\theta I_\theta}}\ (\text{rotational damping ratio}) \tag{13}$$

$$U_\theta = \frac{U}{f_{n\theta}D}\ (\text{rotational reduced velocity}) \tag{14}$$

$$f_{n\theta} = \frac{1}{2\pi}\sqrt{\frac{K_\theta}{I_\theta}}\ (\text{rotational natural frequency, changed with } U_\theta) \tag{15}$$

$$C_M = \frac{2M_\theta}{\rho D^2 U^2}\ (\text{pitching moment coefficient}) \tag{16}$$

$$I_\theta^* = \frac{I_\theta}{\rho D^4}\ (\text{mass moment of inertia}) \tag{17}$$

The coupled responses of flow-induced vibration and rotation are solved using the ANSYS-FLUENT package, assisted by user-defined functions (UDF). The finite volume method (FVM) is used to discretize the Navier-Stokes equations. To achieve pressure-velocity coupling, a coupled scheme is adopted based on the overset mesh method. In each time step, the flow-induced lift force and moment exerted on the cylinder-plate body are calculated by integrating the pressure and viscous stress components, after the flow field is obtained by solving the dimensional forms of Eqs. (1) and (2). Then, Eqs. (3) and (11) are solved using an improved fourth-order Runge-Kutta method (Zhu et al., 2021a; Tang et al., 2023b). Accordingly, the cylinder-plate body moves to a new position and the computational mesh is updated for the calculation of the flow field in the subsequent time step.

Table 2
Convergence analysis on mesh density.

Mesh	Elements in background domain	Elements in overlapping domain	$\overline{Y}$	Y_A	$\overline{\theta}$	θ_A
Coarse	40900	49370	0.00667	0.79544	0.00662	0.68398
Fine	53200	66150	0.00679 (1.80%)	0.81199 (2.08%)	0.00672 (1.51%)	0.71209 (4.11%)
High-resolution	78800	84280	0.00685 (0.88%)	0.81532 (0.41%)	0.00678 (0.89%)	0.72170 (1.35%)

Table 3
Convergence analysis on time-step.

Time-step	$\overline{Y}$	Y_A	$\overline{\theta}$	θ_A
0.01s	0.00665	0.79740	0.00647	0.70150
0.005s	0.00679 (2.11%)	0.81199 (1.83%)	0.00672 (3.86%)	0.71209 (1.51%)
0.0025s	0.00683 (0.59%)	0.81281 (0.10%)	0.00679 (1.04%)	0.71458 (0.35%)

2.3. Convergence analysis and computational mesh

In the present two-dimensional simulations, a rectangular background domain with a length of 60*D* and a width of 40*D* is utilized, as depicted in Fig. 2. The distances from the center of the circular cylinder to the upstream boundary and the two bilateral boundaries are all 20*D*. To ensure accurate calculations, a concentric circle containing the cylinder-plate body is specified as the overlapping domain. A dependence study is performed to identify the diameter of the concentric circle, and the results are shown in Table 1 where the values in parentheses represent the relative differences between the results obtained in the current and preceding row. It can be seen that the differences become smaller with increasing the circle diameter from 18*D* to 22*D*, implying that the numerical results gradually converge to stable values. As the differences between the group of 20*D* and 22*D* are less than 1%, demonstrating that the improvement of numerical results is negligible, therefore the diameter of the concentric circle is determined as 20*D* for further simulations. Regarding the boundary conditions, a steady uniform velocity is applied at the inlet. The pressure-outlet condition is set at the downstream boundary to ensure a fully developed flow. At the two lateral boundaries, the normal component of the velocity and the tangential component of the wall shear stress are set to zero. A no-slip wall condition is specified on the structure surface. The overset boundary condition is applied at the borderline between the background and overlapping domain.

The convergence analysis on mesh density and time-step is conducted for the same case of the cylinder-plate body at $U_y = 8$ and $U_\theta = 8$. Three types of mesh grids, namely coarse, fine, and high-resolution, are employed for both the overlapping and background domain, as presented in Table 2. The results indicate that values of $\overline{Y}$, Y_A, $\overline{\theta}$, and θ_A exhibit minimal changes when transitioning from fine to high-resolution grids. Here, $\overline{Y}$, Y_A, $\overline{\theta}$, and θ_A denote the time-averaged vibration displacement, the vibration amplitude, the time-averaged rotation angle, and the rotary amplitude, respectively. As shown in Table 2, the maximum difference between the group of fine and high-resolution grids is 1.35%, and all other differences are less than 1%, which means that the computed results are not improved much with further refining the mesh density. Therefore, the mesh system with fine grids is employed to resolve the flow field around the cylinder-plate body. With this mesh resolution, the height of the first-layer mesh near the structure surface is $\Delta y = 0.005D$. The time-step independence validation is conducted under three different time-steps (0.01s/0.005s/0.0025s), as shown in Table 3. Similarly, considering computational efficiency, a time-step of 0.005s is chosen, as the relative differences between the results obtained with 0.005s and 0.0025s are negligible. Since the mesh system used in this study remains consistent across all other cases, no further analyses are required.

2.4. Numerical model validation

To validate the numerical methods described above, the individual flow-induced vibration and rotation responses of a cylinder-plate body are investigated. As shown in Fig. 3(a), in the range of U_y = 2–6, the vibration amplitudes change very little (nearly zero) and the associated frequencies show a linear relationship, presenting VIV-type oscillations. As U_y increases, the amplitudes build up with U_y at high vibrational

Table 4
Setups of present studying cases.

Cases	Re	U_y	$m^*\zeta_y$	U_θ	$I^*\zeta_\theta$	Section
FIV-only	120	3–18	0.069	/	/	3.1
FIR-only	120	/	/	3–18	0.001426	3.1
Coupled responses of FIV and FIR	120	3–18	0.069	5, 8, 12, 18	0.001426	3.2–3.5

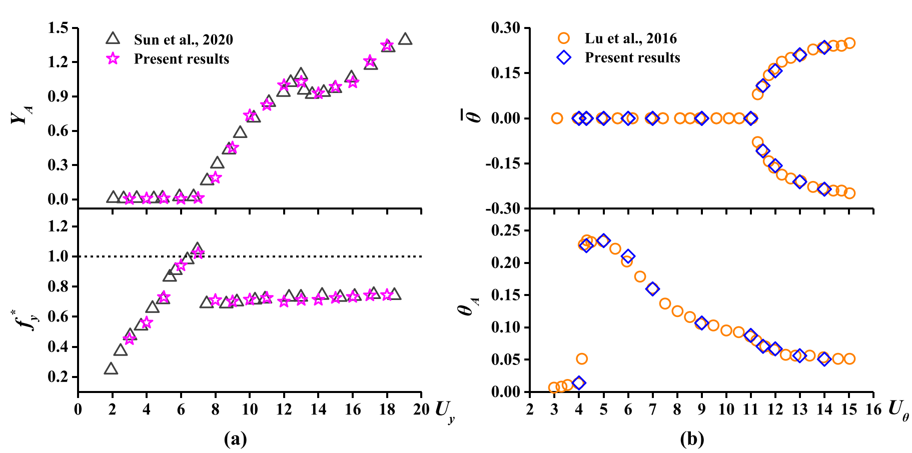

Fig. 3. Responses of a circular cylinder attached with a 1*D* splitter plate: (a) the normalized vibration amplitudes (Y_A) and frequencies ($f_y^* = f_y/f_{ny}$, where f_y is the vibration frequency) at Re = 100, $m^* = 10$, and $\zeta_y = 0$; (b) the time-averaged rotation angles ($\overline{\theta}$) and rotary amplitudes (θ_A) at Re = 100, $m^* = 10$, and $\zeta_\theta = 0.007$.

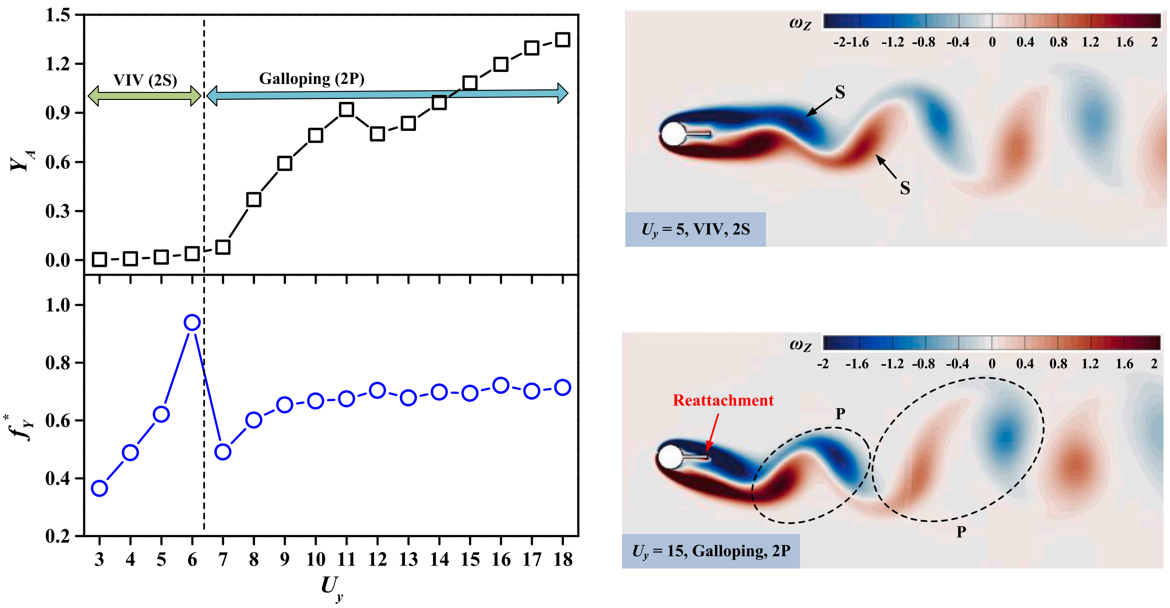

(a) (b)

Fig. 4. Vibration responses of the cylinder-plate body: (a) amplitudes and frequencies; (b) instantaneous vorticity field when the structure returns to the equilibrium location during the upward motion.

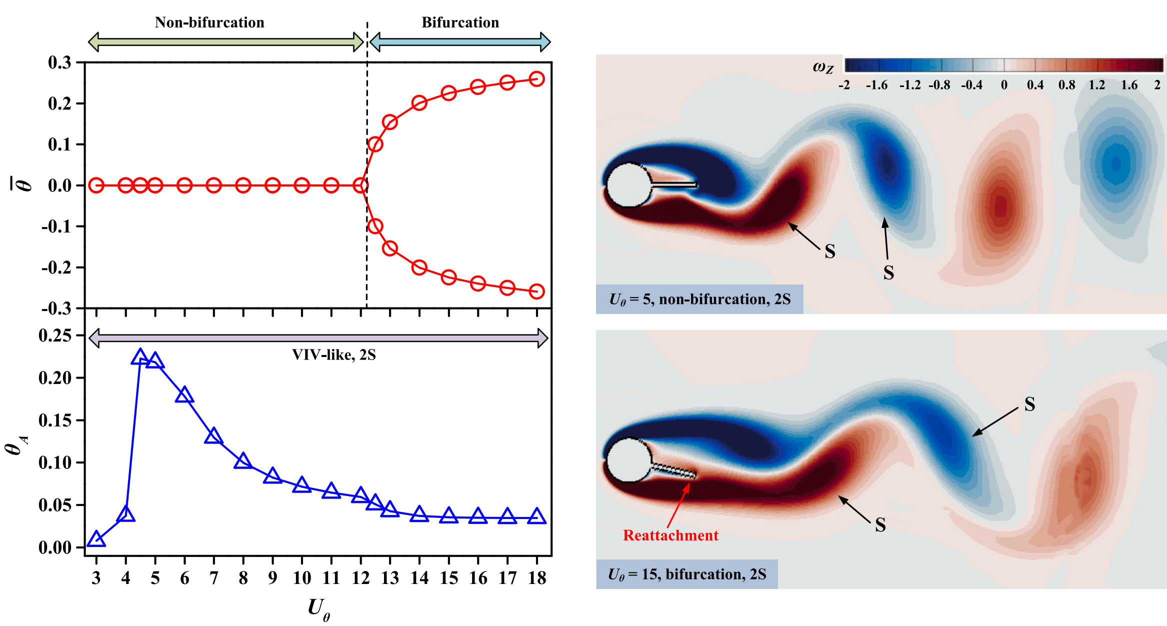

(a) (b)

Fig. 5. Rotation responses of the cylinder-plate body: (a) time-averaged rotation angles $\bar{\theta}$ and rotary amplitudes θ_A; (b) instantaneous vorticity field when the structure returns to the equilibrium location during the anti-clockwise motion.

reduced velocities. Additionally, the vibration frequencies do not synchronize with the natural frequency but transitions to a lower frequency branch, showing typical galloping-type responses. To further verify the numerical model, the flow-induced rotation responses of a cylinder-plate body are also examined and compared, as depicted in Fig. 3(b). The numerical results demonstrate that, in the band of $U_\theta \leq 11$, the rotary oscillations of the cylinder-plate body behave strictly symmetric with respect to the flow direction, i.e., $\bar{\theta} = 0$. However, a bifurcation phenomenon occurs as the rotational reduced velocity exceeds 11, giving rise to a net deflection to either positive or negative side. The variations of θ_A v.s. U_θ present a VIV-like response, characterized by small amplitudes at low reduced velocities, followed by a sudden increase, a subsequent decrease, and finally converging to a certain value. In general, the present mathematical model and numerical method can provide an accurate prediction.

3. Results and discussion

To provide a clear discussion routine, the considered cases in this work are organized as shown in Table 4.

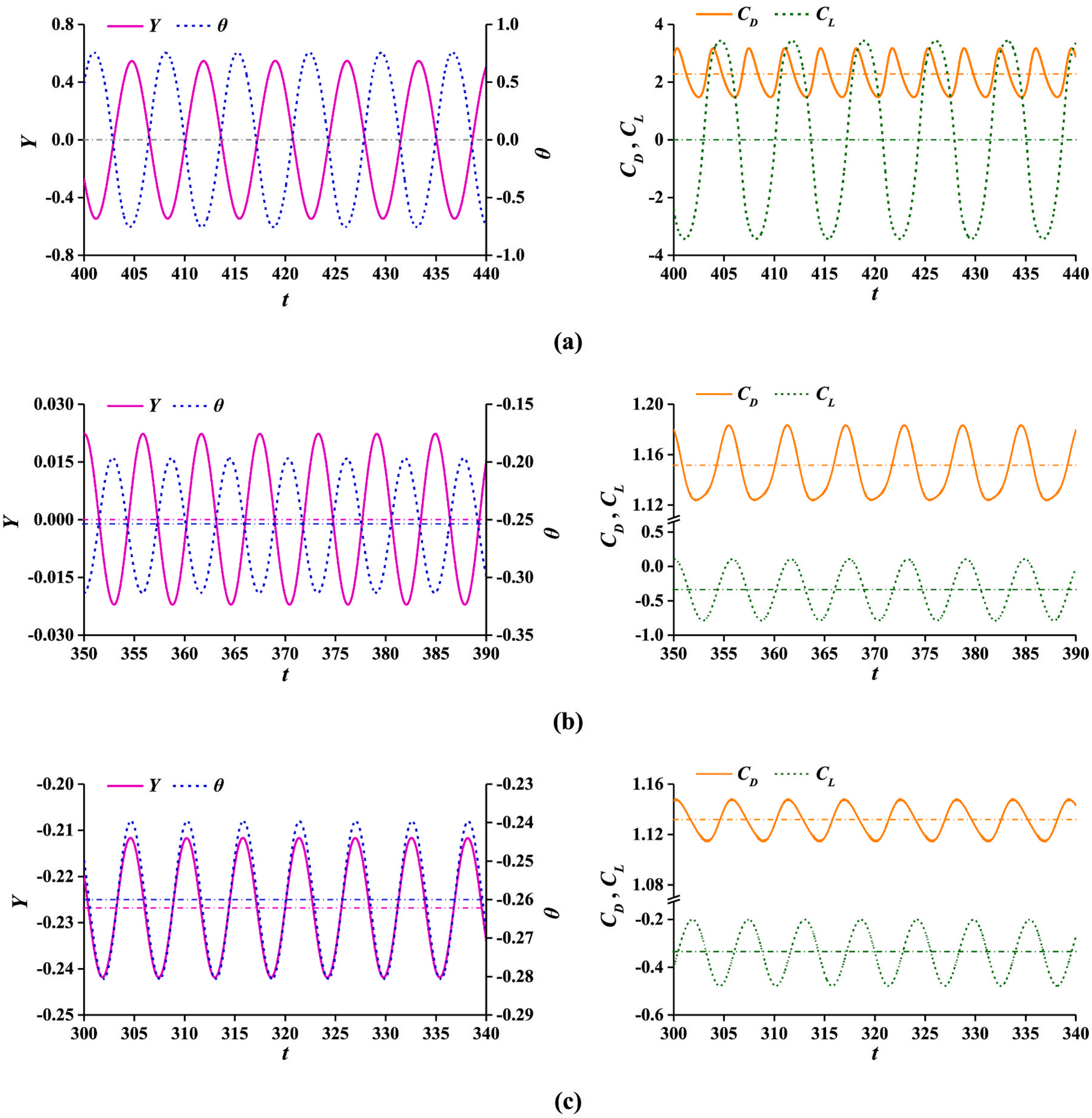

Fig. 6. Time histories of displacements, rotation angles, drag coefficients, and lift coefficients: (a) non-bifurcation responses at $U_\theta = 18$ and $U_y = 6$; (b) bifurcation only in rotation responses at $U_\theta = 18$ and $U_y = 4$; (c) bifurcation in both vibration and rotation responses at $U_\theta = 18$ and $U_y = 18$.

A fixed Reynolds number is selected for all simulations. According to Xie et al. (2012), investigations on flow-induced motions are usually conducted by changing either the reduced velocity (thus the Reynolds number) or the frequency ratio. Experimentally, the inflow velocity of the wind or water tunnel can be conveniently changed. However, in numerical simulations, varying the structure's natural frequency is preferred. This method has been widely used by other researchers (Bhatt and Alam, 2018; Lu et al., 2016; Sahu et al., 2019; Zhang et al., 2021; Chen et al., 2020; Zhao, 2013) in VIV's numerical studies and it is also adopted in this paper, i.e., the natural frequency of the cylinder-plate body is set as a variable to cover the reduced velocity range of 3–18.

The specific low Reynolds number of 120 is employed based on the following three reasons. 1) The wake flow behind a circular cylinder has negligible three-dimensional turbulent characteristics when Re $\leq$ 190 (Carmo and Meneghini, 2006). Therefore, the present numerical model for Re = 120 can be studied using two-dimensional numerical simulations. Comparing with three-dimensional simulation, the computational cost of two-dimensional study can be significantly reduced. Furthermore, the results at lower Reynolds numbers could provide a clear picture of flow wake including the boundary layer development and separation points, subsequently a useful guidance for the forthcoming three-dimensional study. 2) The low Reynolds number flow can be found around the seabed. Incorporating the cylinder-plate body within the seabed environment presents a dual advantage encompassing energy harvesting capabilities while maintaining minimal interference with both maritime navigation and marine ecosystems. 3) The examination of the basic fluid-structure interaction mechanics at low Reynolds numbers is a common choice (Bhatt and Alam, 2018; Lu et al., 2016; Sahu et al., 2019; Zhang et al., 2021; Chen et al., 2020; Zhao, 2013) because of the low cost and useful reference.

A wide reduced velocity range of 3–18 is selected for both the FIV-only and FIR-only cases. This is because typical vibration responses including VIV, transition from VIV to galloping, and galloping for the FIV-only cases (Tang et al., 2023a; Sun et al., 2020; Liang et al., 2018), and the rotational bifurcation phenomenon for the FIR-only cases (Lu et al., 2016; Zhang et al., 2021; Tang et al., 2022a) can be observed in the present reduced velocity range of 3–18. For the coupled responses, we mainly focus on the effects of FIR on FIV responses, so the vibrational

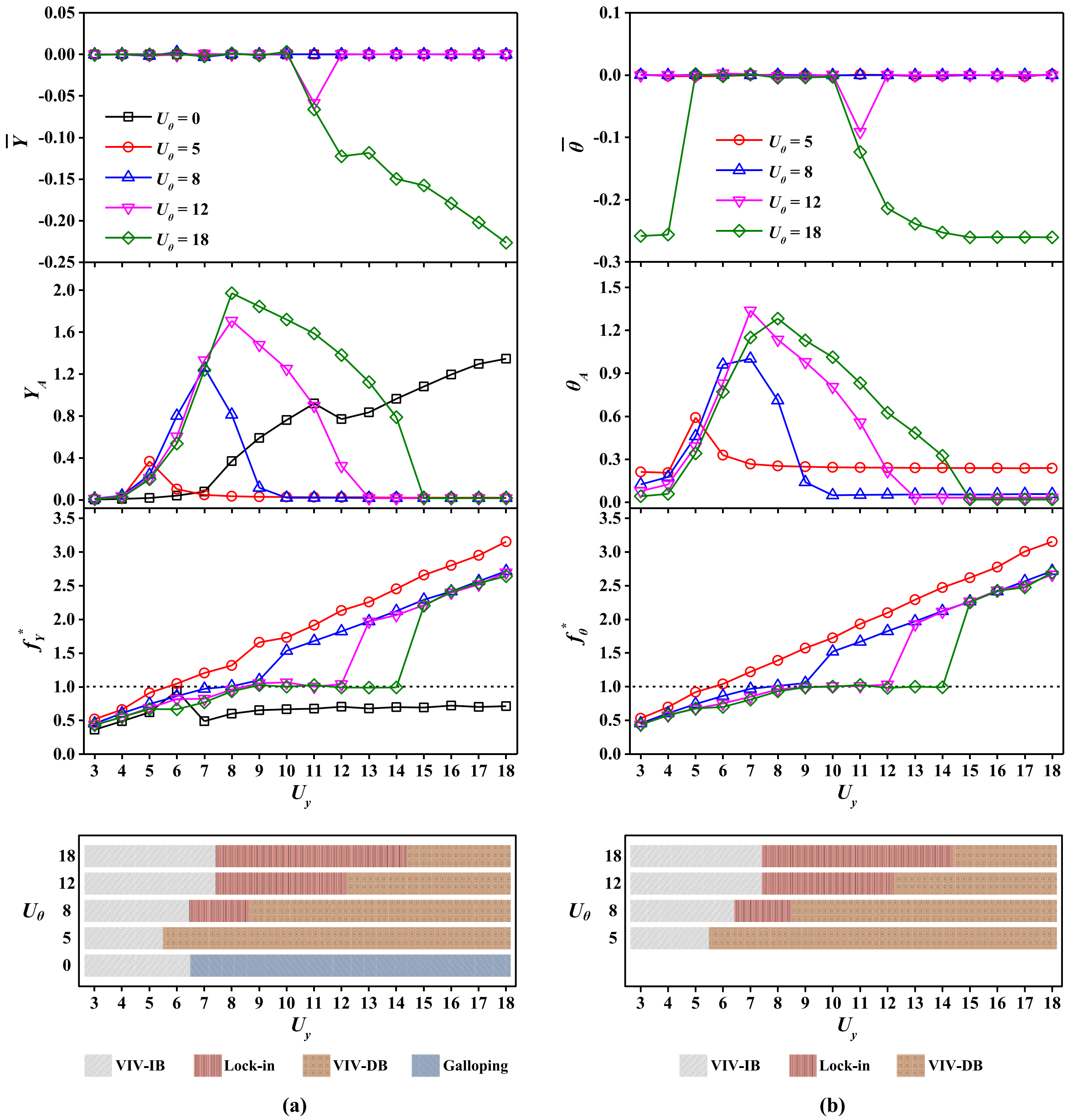

Fig. 7. Variations of the time-averaged values ($\overline{Y}$ and $\overline{\theta}$), amplitudes (Y_A and θ_A), frequencies ($f_y{}^*$ and $f_\theta{}^*$, where $f_\theta{}^* = f_\theta/f_{n\theta}$ and f_θ is the rotation frequency), and oscillation modes: (a) vibration responses; (b) rotation responses.

reduced velocity range of $U_y = 3$–18 is kept the same as the FIV-only cases while four typical rotational reduced velocities of $U_\theta = 5$, 8, 12, and 18 are chosen to cover the significant rotational characteristics such as bifurcation and large rotation amplitude which can be observed in Section 3.1.

The mass-damping ratio ($m^*\zeta_y$) is kept the same as our previous work (Tang et al., 2023a). The mass moment of inertia I^* can be accordingly obtained after the mass and the size of the cylinder-plate body are identified, and the rotational damping constant of $\zeta_\theta = 0.001$ is adopted to ensure the large-amplitude rotation responses.

3.1. Vibration-only and rotation-only cases

Prior to investigating the coupled responses of flow-induced vibration and rotation, it is essential to establish benchmark cases by examining the individual vibration and rotation of the cylinder-plate body. These benchmark cases serve as reference points for comparisons and provide valuable insights. Fig. 4(a) illustrates a full interaction between VIV and galloping for the present cylinder-plate body under the specified conditions of $m^*\zeta_y = 0.069$ and Re = 120. The transition between VIV and galloping occurs within the U_y range of 6–7. Notably, a slight reduction in amplitudes appears when U_y increases from 11 to 12, forming the "kinks" (Miyata et al., 1983; Bearman et al., 1987; Mannini et al., 2014; Zhao et al., 2014). The 2S (two isolated vortices) and 2P (two pairs of vortices) vortex shedding mode are observed in the VIV and galloping branch, respectively. As shown in Fig. 4(b), at $U_y = 5$ in the VIV region, the shear layer originating from the upper surface of the circular cylinder passes over the splitter plate and forms vortices behind it, resulting in the 2S mode. By contrast, at $U_y = 15$ in the galloping region, the shear layer reattaches to the splitter plate surface, introducing an asymmetric pressure distribution along the two sides of the splitter plate. This significant asymmetry generates extra fluid forces acting on the plate (Zhu et al., 2020a), leading to galloping responses and the corresponding 2P vortex shedding mode.

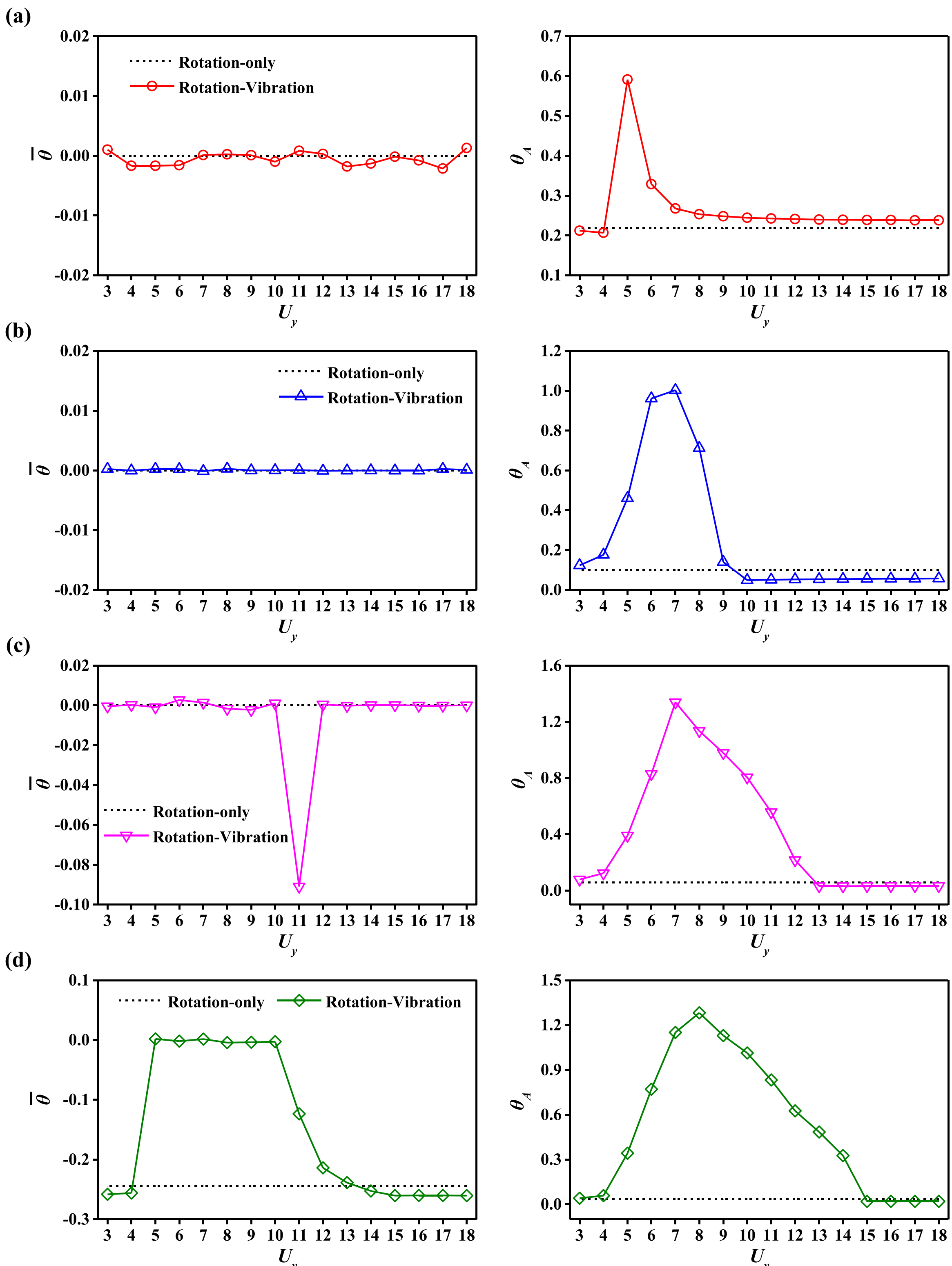

Fig. 8. Comparisons of the time-averaged rotation angles and rotary amplitudes between the rotation-only case and the coupled cases: (a) $U_\theta = 5$; (b) $U_\theta = 8$; (c) $U_\theta = 12$; (d) $U_\theta = 18$.

We further investigate the flow-induced rotation responses of the cylinder-plate body at $I^*\zeta_\theta = 0.001426$ and Re = 120, and the results are presented in Fig. 5. A bifurcation phenomenon is observed in the band of $U_\theta > 12$, where an increase in U_θ leads to a lager $\overline{\theta}$. The rotary amplitudes are relatively small in the range of $U_\theta \leq 4$. However, a distinct behavior appears at $U_\theta = 5$, where the rotary amplitudes exhibits a sudden increase, followed by a decrease as U_θ further increases. Eventually, the amplitudes stabilize at a nearly constant value of approximately $\theta_A = 0.034$ in the range of $14 \leq U_\theta \leq 18$. The variation of θ_A with respect to U_θ indicates a VIV-like rotational mode. Fig. 5(b) demonstrates the 2S

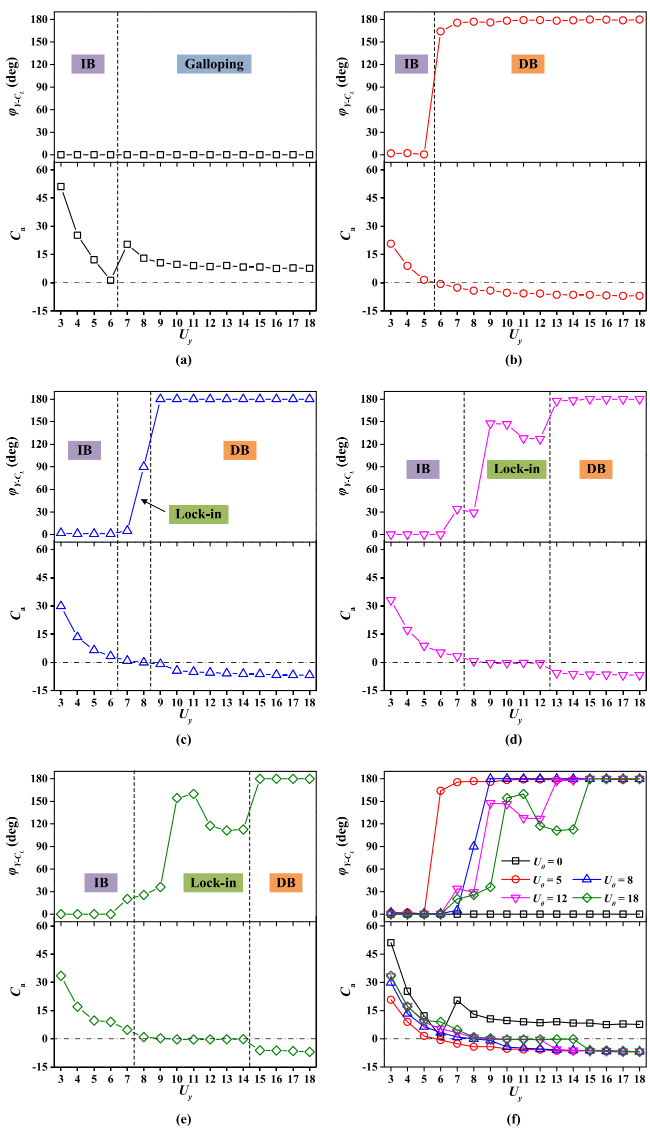

Fig. 9. Phase differences (displacements versus lift coefficients) and the added mass coefficients: (a) $U_\theta = 0$; (b) $U_\theta = 5$; (c) $U_\theta = 8$; (d) $U_\theta = 12$; (e) $U_\theta = 18$; (f) the overall comparisons.

vortex shedding mode throughout the whole range of $U_\theta = 3$–18. However, notable differences can be found between the 2S mode in the non-bifurcation and bifurcation region. At $U_\theta = 5$, when the cylinder-plate body rotates with a center-line of $\overline{\theta} = 0$, two identical vortices are alternately shed from two sides of the body. In contrast, when the cylinder-plate body deflects to the negative position at $U_\theta = 15$, the shear layer from the lower surface of the circular cylinder reattaches to the splitter plate. This reattachment behavior results in an elongated vortex formation length and the generation of two different vortices.

3.2. Coupled responses

Based on the appearance of the bifurcation phenomenon, the coupled responses of flow-induced vibration and rotation for the cylinder-plate body can be classified into three distinct types, as illus-

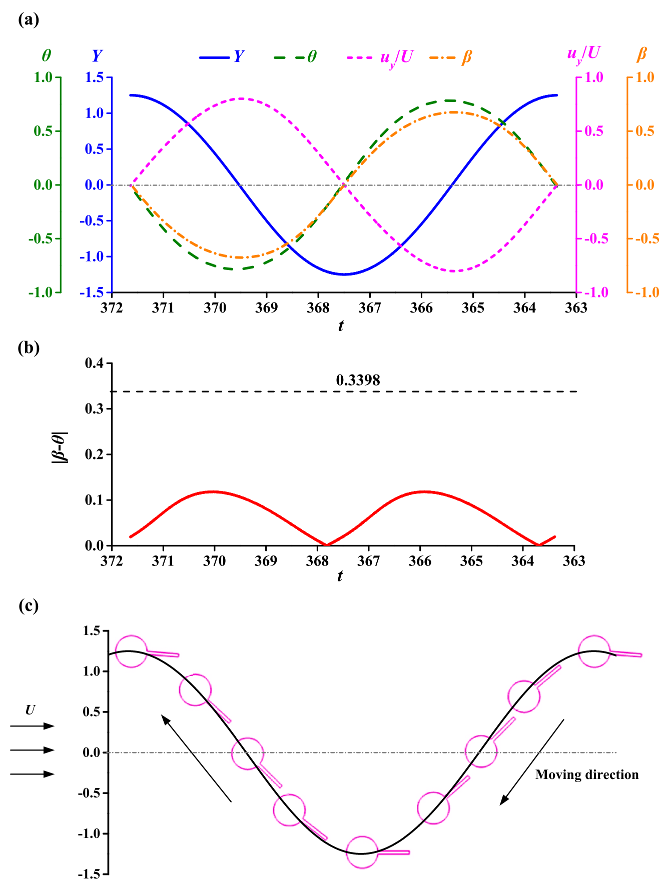

Fig. 11. Coupled movements at $U_\theta = 12$ and $U_y = 10$, where the phase difference between Y and θ equals to nearly 90°: (a) time histories of Y, θ, u_y/U, and β; (b) absolute values of β-θ; (c) the structural postures in one vibration period.

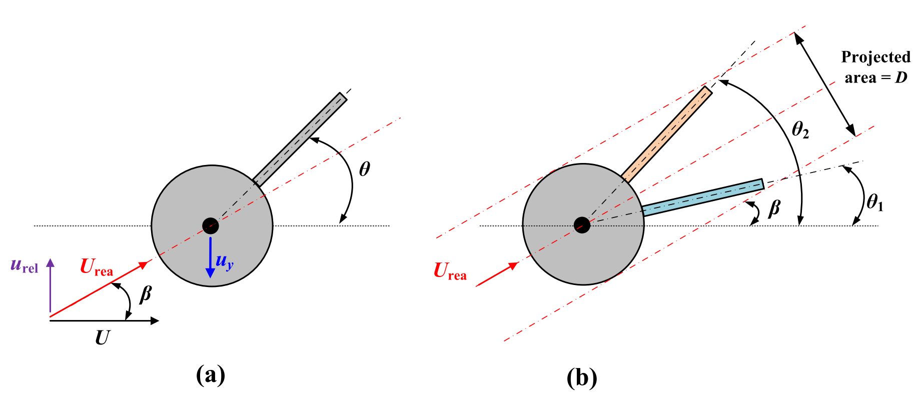

Fig. 10. (a) Definition of angle β; (b) conditions that the projected area is no more than D.

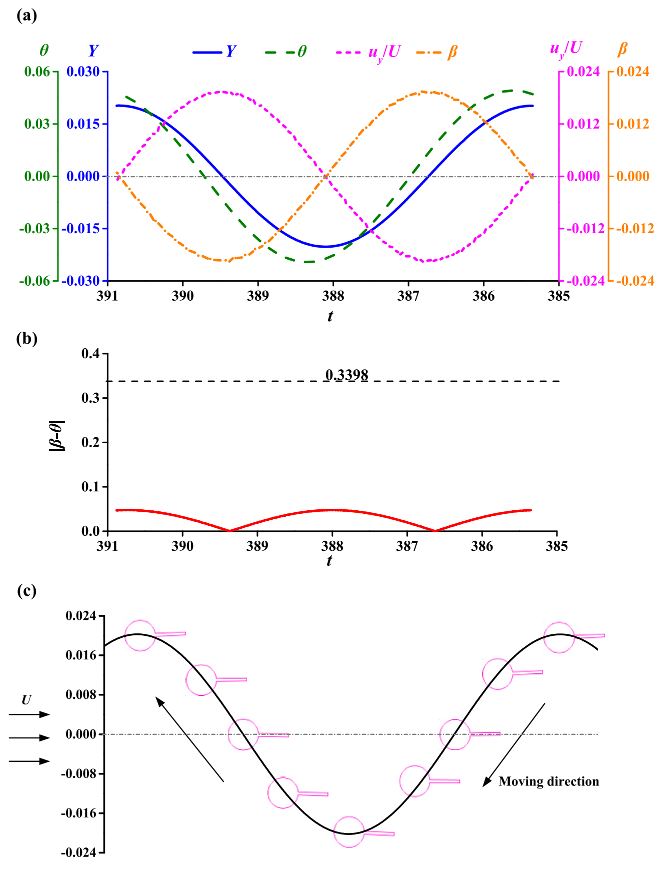

Fig. 12. Coupled movements at $U_\theta = 8$ and $U_y = 10$, where the phase difference between Y and θ equals to nearly 0°: (a) time histories of Y, θ, u_y/U, and β; (b) absolute values of β-θ; (c) the structural postures in one vibration period.

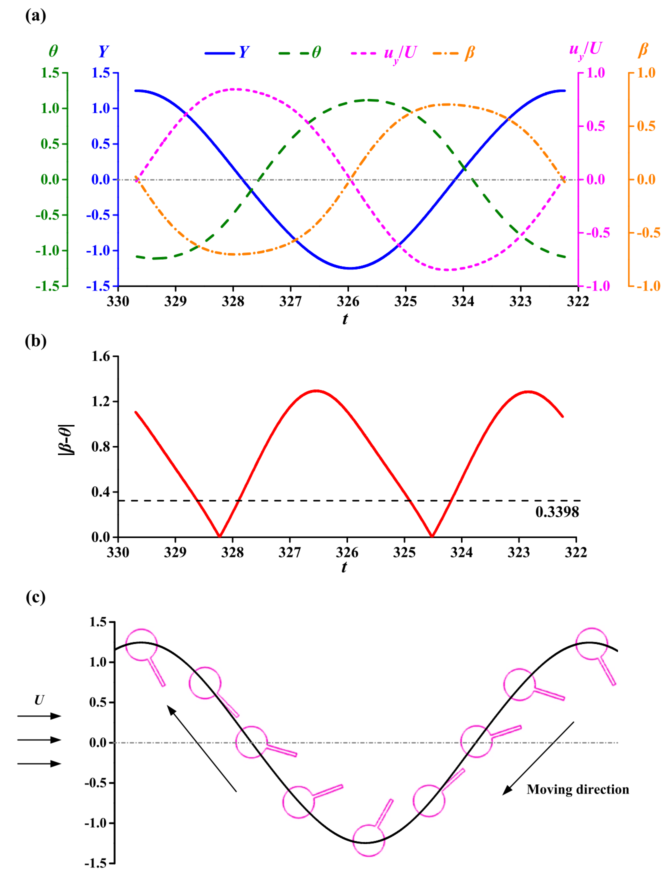

Fig. 13. Coupled movements at $U_\theta = 18$ and $U_y = 7$, where the phase difference between Y and θ equals to nearly 180°: (a) time histories of Y, θ, u_y/U, and β; (b) absolute values of β-θ; (c) the structural postures in one vibration period.

trated in Fig. 6. These categories include non-bifurcation responses, bifurcation only in rotation responses, and bifurcation in both vibration and rotation responses. Fig. 6(a) depicts well-organized and harmonic oscillations characterized by $\overline{Y} = 0$ and $\overline{\theta} = 0$, which signify non-bifurcation responses. In this case, the cylinder-plate body vibrates and rotates around an equilibrium position parallel to the oncoming flow, consequently leading to $\overline{C}_L = 0$. Conversely, Fig. 6(b) demonstrates a configuration of $\overline{Y} = 0$ while $\overline{\theta} \neq 0$, indicating the occurrence of bifurcation solely in the rotation responses. As the cylinder-plate body does not rotate around $\theta = 0$, the time histories of lift coefficients exhibit fluctuations around a non-zero value ($\overline{C}_L \neq 0$), further confirming the symmetry-breaking bifurcation. In the third response shown in Fig. 6(c), the cylinder-plate body exhibits deflections in both vibrational and rotational directions, characterized by $\overline{Y} \neq 0$ and $\overline{\theta} \neq 0$. From the above observations, it can be concluded that the bifurcation in rotation responses does not guarantee the appearance of vibrational bifurcation. However, it certainly leads to $\overline{C}_L \neq 0$, demonstrating that the non-zero time-averaged lift forces are achieved once the symmetrical configuration is broken.

Fig. 7 presents a comparative analysis of the time-averaged values, amplitudes, frequencies, and oscillation modes for both vibration and rotation responses at different rotational reduced velocities. To understand the influence of rotational motions on vibration responses, the reference group with $U_\theta = 0$ (vibration-only) is also plotted. At $U_\theta = 0$, 5, and 8, the values of $\overline{Y}$ and $\overline{\theta}$ remain close to zero across the entire U_y range, indicating non-bifurcation responses. However, for $U_\theta = 12$, the negative $\overline{Y}$ and $\overline{\theta}$ appear at $U_y = 11$, confirming the bifurcation in both vibrational and rotational directions. More pronounced bifurcations are observed at $U_\theta = 18$. The cylinder-plate body does not deflect to neither positive or negative positions in the range of $U_y = 3$–10, leading to $\overline{Y} = 0$. However, in a large U_y range of 11–18, $\overline{Y} < 0$ can be clearly observed, showing that the cylinder-plate body has deflected to a negative equilibrium position. It is worth noting that the magnitude of the negative $\overline{Y}$ increases as U_y increases, with the maximum value $\overline{Y} = -0.2266$ occurring at $U_y = 18$. Bifurcation in the rotational responses is also observed in the range of $U_y = 11$–18, where the negative $\overline{\theta}$ experiences a sharp increase from $U_y = 11$ to 14 but remains nearly unchanged ($\overline{\theta} = -0.26$) for the remaining U_y range. Additionally, a rotational bifurcation ($\overline{\theta} = -0.256$) is observed at $U_y = 3$–4, which causes bifurcation solely in rotation responses, as shown in Fig. 6(b).

The full interaction between VIV and galloping has been identified for the case of $U_\theta = 0$, and the details can be referred in Fig. 4. However, when considering passive rotations, the flow-induced vibration responses undergo significant changes. As demonstrated in Fig. 7(a), the curves of Y_A versus U_y and f_Y* versus U_y reveal typical VIV modes for $U_\theta = 5$, 8, 12, and 18. Specifically, at $U_\theta = 5$, IB-DB mode is observed without a distinct lock-in regime, where IB and DB are the VIV initial and desynchronization branch, respectively. By comparison, IB-(lock-in)-DB mode is identified at $U_\theta = 8$, 12, and 18. In general, with an increase in U_θ, the peak vibration amplitudes escalate ($Y_A = 0.367$, 1.259, 1.708, and 1.972 for $U_\theta = 5$, 8, 12, and 18, respectively), the onset U_y of the lock-in region shifts to higher values ($U_y = 7$, 8, and 8 for $U_\theta = 8$, 12, and 18, respectively), and the lock-in region becomes wider ($U_y = 7$–8, 8–12, and 8–14 for $U_\theta = 8$, 12, and 18, respectively). It is important to note that within the lock-in region, the vibration amplitudes of coupled responses are generally larger than those at $U_\theta = 0$, indicating the enhancement in flow-induced vibrations under the passive rotations. This behavior holds potential for applications in the field of renewable

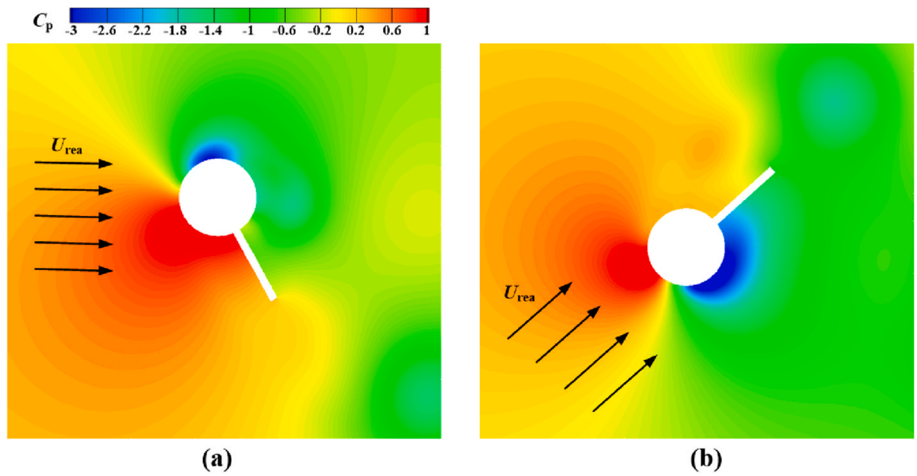

Fig. 14. Typical distribution of pressure coefficients at $U_\theta = 18$ and $U_y = 7$: (a) $t = 322.2375$, $\theta = -1.08925$, $\beta = -0.02333$; (b) $t = 324.5$, $\theta = 0.67887$, $\beta = 0.69474$.

energy harvesting. However, in the DB regime for $U_\theta = 5$, 8, 12, and 18, the vibration amplitudes are close to zero, considerably smaller than those observed in the galloping when $U_\theta = 0$. This signifies a mitigation effect. Regarding the rotation responses in Fig. 7(b), similar VIV-like modes including IB, lock-in, and DB are observed.

Fig. 8 presents a comparison of the time-averaged rotation angles and rotary amplitudes between the rotation-only case (represented by black dashed lines) and the coupled cases (indicated by colored lines with symbols) to illustrate the influence of flow-induced vibrations on passive rotation responses. For $U_\theta = 5$ and 8 in Fig. 8(a) and (b), respectively, the vibration effects on rotation responses are not significant, as $\overline{\theta}$ for the coupled cases closely aligns with that of the rotation-only case in the whole U_y range, i.e., $\overline{\theta} \approx 0$. By contrast, for larger rotational reduced velocities, the rotary equilibrium positions are clearly altered in specific U_y ranges. As shown in Fig. 8(c), the coupled case exhibits non-bifurcation responses ($\overline{\theta} \approx 0$) in the U_y range of 3–10 and 12–18, consistent with the results obtained in the rotation-only case. However, at $U_y = 11$, the negative value of $\overline{\theta} = -0.09$ shows a bifurcation behavior. In Fig. 8(d), the cylinder-plate body, without considering the flow-induced vibration, deflects to a negative equilibrium position ($\overline{\theta} = -0.2442$). The variations of $\overline{\theta}$ for the coupled case deviate from the baseline of $\overline{\theta} = -0.2442$, showing several distinct steps: (1) remains nearly unchanged in $U_y = 3$–4 and slightly lower than the baseline; (2) an abrupt jump to $\overline{\theta} = 0$ is observed at $U_y = 5$, indicating a non-bifurcation characteristic, and this value is maintained as U_y increases up to 10; (3) a rapid drop from $\overline{\theta} = 0$ to $\overline{\theta} = -0.253$ occurs in $U_y = 10$–14, showing the reemergence of bifurcation; and (4) $\overline{\theta} = -0.26$ is observed in the remaining U_y range of 15–18. The variations of θ_A versus U_y in the right column indicate that the rotary amplitudes of the coupled cases are similar to those of the rotation-only case in the small and large U_y range. However, significant differences can be observed in the middle U_y range, where the amplitudes of coupled cases are obviously larger than those of rotation-only cases. In conclusion, the above results suggest that flow-induced vibrations exert a significant influence on the rotation responses of the cylinder-plate body. The influenced U_y range is generally dependent on U_θ. A wider U_y range can be observed as U_θ increases, namely $U_y = 5$–8, 4–9, 4–12, and 5–14 for $U_\theta = 5$, 8, 12 and 18, respectively.

3.3. Phase differences

Fig. 9 plots the phase differences (φ_{Y-C_L}, displacements versus lift coefficients) and the associate added mass coefficients (C_a) as a function of U_y. For the vibration-only case ($U_\theta = 0$) in Fig. 9(a), the phase differences remain at $\varphi_{Y-C_L} = 0°$. The C_a curve exhibits a distinct pattern: an initial decrease in the IB region ($U_y \le 6$), followed by a sharp increase at $U_y = 6$–7, which corresponds to the transition from VIV to galloping, and finally a gradual decrease in the galloping region ($U_y = 7$–18). As the phase remains constant at $\varphi_{Y-C_L} = 0°$, the C_a values at $U_\theta = 0$ are consistently positive. When considering the coupled responses, as shown in Fig. 9(b) ~ 10(e), the phase differences undergo a distinct jump from 0° to 180°, resulting in a switch of C_a from positive to negative values. This phase jump is a characteristic feature of VIV (Assi and Bearman, 2015; Gsell et al., 2016). Comparative results in Fig. 9(f) reveal a close relationship between the U_y range of phase jump and U_θ. Specifically, the larger the U_θ, the wider the U_y range of phase jump. Additionally, it should be noted that the process of phase jump for the coupled responses is more intricate compared to the smooth jump behavior observed in the vibration-only case for a bare cylinder (Sun et al., 2020, 2022; Zhu et al., 2020a). Moreover, this circuitous process becomes more pronounced as U_θ increases. For instance, considering the case of $U_\theta = 18$ in Fig. 9(e), the variations of φ_{Y-C_L} can be summarized as follows: (1) remaining at zero in $U_y = 3$–6; (2) exhibiting a nearly linear increase from $U_y = 6$ to 9; (3) experiencing an abrupt jump to $\varphi_{Y-C_L} \approx 150°$ at $U_y = 10$; (4) entering a lower valley region of $\varphi_{Y-C_L} \approx 110°$ in $U_y = 12$–14; and (5) reaching $\varphi_{Y-C_L} = 180°$ in the rest U_y range of 15–18. Referring to Fig. 9 (f), it is clearly seen that the lift coefficients and vibration displacements of the cylinder-plate body can exhibit in-phase, out-of-phase, or intermediate behavior in the VIV region, while they remain constantly in-phase in the galloping region.

Referring to Fig. 6, it can be found that phase differences exist between the displacement and rotation angle, such as $\varphi_{Y-\theta} \approx 180°$ in Fig. 6 (a) and $\varphi_{Y-\theta} \approx 0°$ in Fig. 6(c). The phase differences actually reveal different dynamic characteristics of the coupled responses. Therefore, it is necessary to discuss the relationship between flow-induced motions and phase differences. Firstly, let's introduce the concept of the "real oncoming flow" and discuss the conditions under which the cylinder-plate body assumes a streamlined profile. Here, a streamlined profile refers to a state where the splitter plate remains positioned behind the circular cylinder relative to the "real oncoming flow", without direct contact with it. As displayed in Fig. 10(a), when the cylinder-plate body moves downward with a velocity u_y, it induces a relative velocity u_{rel} in the fluid. Consequently, the real oncoming flow velocity U_{rea} and the angle β between U_{rea} and U can be expressed as:

$$\begin{cases} U_{rea} = \sqrt{U^2 + {u_{rel}}^2} \\ \beta = \arctan \dfrac{u_{rel}}{U} \end{cases} \tag{18}$$

To keep the streamlined profile, the projected area relative to U_{rea} should be no more than D, as shown in Fig. 10(b). The condition

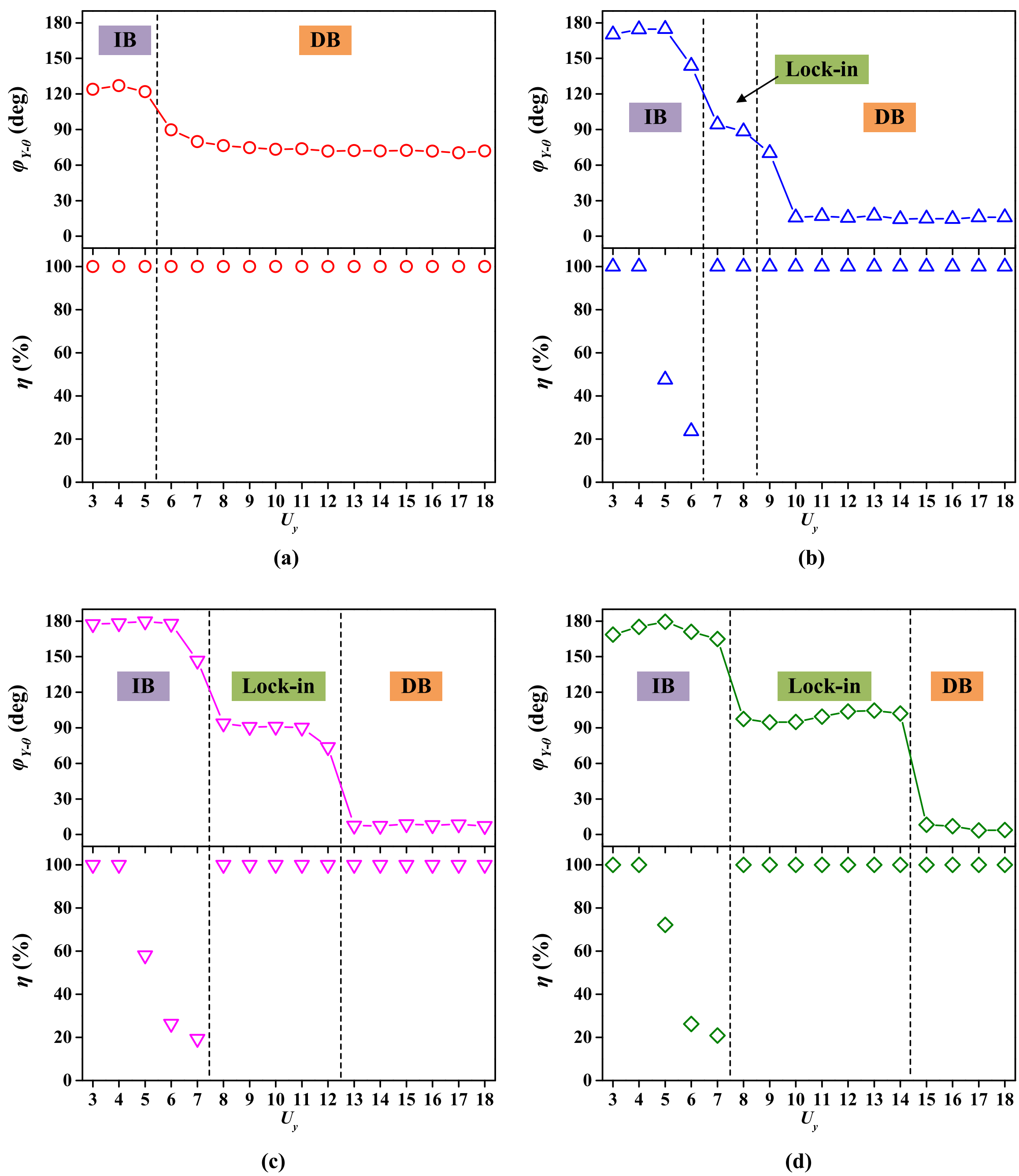

Fig. 15. Variations of phase differences (Y versus θ) and ratios of the time span corresponding to $|\beta-\theta| < 0.3398$ to the entire vibration period: (a) $U_\theta = 5$; (b) $U_\theta = 8$; (c) $U_\theta = 12$; (d) $U_\theta = 18$.

between β and θ should be:

$$\begin{cases} \cos\left(\dfrac{\pi}{2}-\beta+\theta_1\right) = \dfrac{0.5D}{L_{\min}} \quad (L_{\min} \geq L^* + 0.5D) \quad \text{when} \quad \beta > \theta_1 \\ \cos\left(\dfrac{\pi}{2}+\beta-\theta_2\right) = \dfrac{0.5D}{L_{\min}} \quad (L_{\min} \geq L^* + 0.5D) \quad \text{when} \quad \beta < \theta_2 \end{cases} \tag{19}$$

Further, the mathematical expressions are:

$$\begin{cases} \beta-\theta_1 \leq \arcsin\dfrac{1}{1+2L^*} \quad \text{when} \quad \beta > \theta_1 \\ \theta_2-\beta \leq \arcsin\dfrac{1}{1+2L^*} \quad \text{when} \quad \beta < \theta_2 \end{cases} \tag{20}$$

Finally, the unified form is:

$$|\beta-\theta| \leq \arcsin\frac{1}{1+2L^*} \tag{21}$$

Therefore, the moving cylinder-plate body is believed to be streamlined when Eq. (21) is satisfied. For the present cylinder-plate body with $L^* = 1$, Eq. (21) can be written as:

$$|\beta-\theta| \leq \arcsin\frac{1}{3} \quad (0.3398) \tag{22}$$

Figs. 11–13 display the coupled movements in one vibration period for typical cases: $\varphi_{Y-\theta} \approx 90^\circ$, $\varphi_{Y-\theta} \approx 0^\circ$, and $\varphi_{Y-\theta} \approx 180^\circ$, respectively. Each figure consists of three sub-graphs arranged from top to bottom: (a) time histories of Y, θ, u_y/U, and β; (b) absolute values of β-θ, where the critical line of $|\beta-\theta| = 0.3398$ is also plotted; and (c) the instantaneous

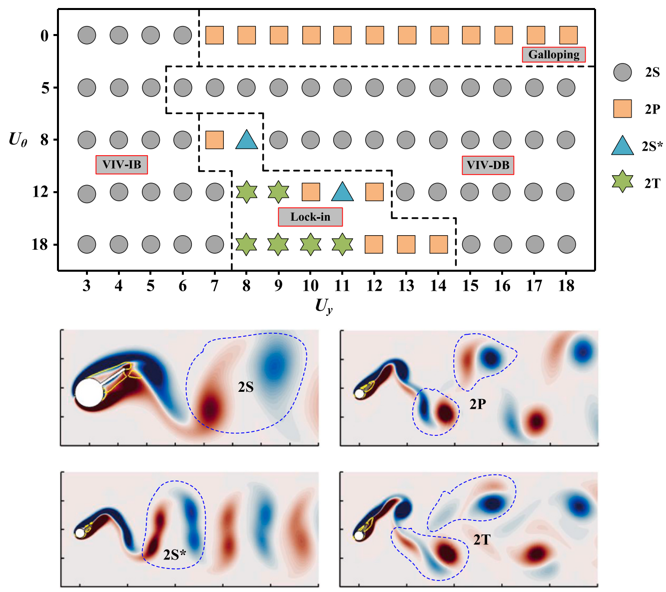

Fig. 16. An overview of wake modes and associated vibration/rotation responses.

structural postures. As depicted in Fig. 11(a), it can be found that θ is nearly zero when the cylinder-plate body reaches its maximum positive position, indicating that θ lags behind Y by approximately 90°. As the phase of Y lags behind u_y/U by nearly 90°, θ and u_y/U are almost out-of-phase. The time history of β follows a similar pattern to that of θ, where they are in-phase and nearly equal. Consequently, the values of $|\beta-\theta|$ in one vibration period are all lower than the critical line of 0.3398, as demonstrated in Fig. 11(b). This indicates that the cylinder-plate body maintains a streamlined profile even with large amplitudes. The instantaneous structural postures depicted in Fig. 11(c) further confirm the streamlined profile. At positions corresponding to the maximum or minimum displacement, U_{rea} is equal to U since the instantaneous moving velocity is zero. At the same time, the cylinder-plate body remains nearly horizontally oriented, resulting in a streamlined profile. Throughout the movement between the maximum positive and negative positions, the splitter plate remains concealed behind the circular cylinder, also leading to a streamlined profile. This dynamic response illustrate that the cylinder-plate body can adjust its posture for the purpose of drag reduction.

In Fig. 12, the phase difference between Y and θ is $\varphi_{Y-\theta} \approx 0^{\circ}$, indicating that Y and θ are almost in-phase. The angle β lags behind θ by nearly 90°. The cylinder-plate body appears to be relatively static, as the vibration and rotation amplitudes are small, not exceeding 0.03 and 0.06, respectively. The small u_y and β are accordingly produced under small-amplitude vibrations and rotations. Consequently, the values of $|\beta-\theta|$ in Fig. 12(b) are all below the line of 0.3398, confirming the streamlined profile. The consecutive frames in Fig. 12(c) illustrate that the cylinder-plate body primarily maintains a horizontal posture, with only minor adjustments in the transverse and torsional directions. This dynamic response also illustrates the achievement in drag reduction.

The coupled movements at $\varphi_{Y-\theta} \approx 180^{\circ}$ depicted in Fig. 13 exhibit greater complexity, as compared with $\varphi_{Y-\theta} \approx 90^{\circ}$ in Fig. 11 and $\varphi_{Y-\theta} \approx 0^{\circ}$ in Fig. 12. The presence of large-amplitude vibrations leads to significant values of u_y, which in turn introduce a substantial β. In contrast to the in-phase relationship observed at $\varphi_{Y-\theta} \approx 90^{\circ}$ in Fig. 11, there is a phase lag of approximately 90° between θ and β when $\varphi_{Y-\theta} \approx 180^{\circ}$. Consequently, the values of $|\beta-\theta|$ no longer remain consistently below the critical value of 0.3398, as demonstrated in Fig. 13(b). Portions of the curve above the line of $|\beta-\theta| = 0.3398$ represent instances where the instantaneous projected area of the cylinder-plate body under the real oncoming flow exceeds the diameter D, resulting in a loss of the streamlined profile. Fig. 13(c) demonstrates that the streamlined profile is briefly achieved when the cylinder-plate body passes through the equilibrium position, but this state is transient and does not persist. At other times, the real oncoming flow appears to dampen the structural movements, particularly in the rotational direction.

To further distinguish the streamlined and non-streamlined profiles, Fig. 14 compares the pressure distributions at two representative instants, which correspond to $|\beta-\theta| > 0.3398$ and $|\beta-\theta| < 0.3398$, respectively. As shown in Fig. 14(a), the real oncoming flow velocity U_{rea} is nearly horizontal, while cylinder-plate body undergoes a clockwise rotation to possess a large rotation angle of $\theta = -1.08925$. Under this configuration, the high-pressure region locates not only along the surface of the cylinder but also on the lower side of the splitter plate. The projected area exceeds D, leading to an increase in drag force. In contrast, Fig. 14(b) illustrates that the high-pressure region is primarily concentrated around the frontal stagnation point of the circular cylinder. Furthermore, the splitter plate is positioned behind the cylinder, avoiding direct exposure to the impact of the real flow U_{rea}. As a result, the streamlined profile is achieved.

Fig. 15 depicts the variations of $\varphi_{Y-\theta}$ and η with various U_y under four different U_θ, where η represents the ratio of the time span corresponding to $|\beta-\theta| < 0.3398$ to the entire vibration period. The results clearly indicate that the variations of $\varphi_{Y-\theta}$ for coupled responses exhibit three typical stages as U_y increases. In Fig. 15(b), (c), and 15(d), corresponding to $U_\theta = 8$, 12, and 18, the phases exhibit $\varphi_{Y-\theta} \approx 180^{\circ}$, $\varphi_{Y-\theta} \approx 90^{\circ}$, and $\varphi_{Y-\theta} \approx 0^{\circ}$ in the IB, lock-in, and DB region, respectively. By contrast, for a lower rotational reduced velocity of $U_\theta = 5$ in Fig. 15(a), $\varphi_{Y-\theta} \approx 120^{\circ}$ and $\varphi_{Y-\theta} \approx 72^{\circ}$ appear in the IB and DB region, respectively, with the absence of the lock-in region and thus the second stage of $\varphi_{Y-\theta} \approx 90^{\circ}$. The results of η versus U_y under various U_θ conditions demonstrate that the cylinder-plate body predominantly maintains a streamlined profile during the coupled movements, as evidenced by $\eta = 100\%$ in most cases. The non-streamlined profile ($\eta < 100\%$) occurs when the oscillation modes are ready to enter into the lock-in region from the IB region, and it becomes more prominent as the oscillation modes approach closer to the lock-in region.

3.4. Vortex shedding modes

Vortex shedding structures in the wake of an elastically mounted body has a significant impact on its vibration/rotation responses. For a light circular cylinder, previous studies by Williamson and Jauvtis (2004) have identified and discussed typical vortex shedding modes, including 2S, 2P, 2C (two pairs of vortices and the same signs for every pair of vortices), and 2T (two triplets of vortices). However, in this work, the 2C mode is not observed, and instead, a new wake mode called 2S* emerges, as shown in Fig. 16. The 2S* mode consists of two single vortices, each of which has the tendency to split into two smaller vortices when migrating downwards. This unique vortex shedding mode can be attributed to the presence of a splitter plate and the coupled responses of flow-induced vibration and rotation. To understand how these wake modes interact with the flow-induced oscillation modes, wake modes (2S, 2P, 2S*, and 2T) and vibration/rotation patterns for the current cylinder-plate body are summarized in Fig. 16. The interaction between VIV and galloping for the vibration-only case ($U_\theta = 0$) has been discussed in Section 3.1. It is observed that the 2S mode dominates in the VIV region, while the 2P mode appears in the galloping region. The shift from 2S to 2P mode actually reflects the decreasing restoring forces as U_y increases, which can be clearly explained by Eqs. (7) and (8). Taking the passive rotations into account, typical VIV oscillation modes including IB, lock-in, and DB are observed, accordingly causing different wake modes. As illustrated in Fig. 16, the 2S mode predominates in the IB and DB region, whereas the 2P, 2S*, and 2T mode are present in the lock-in region. The appearance of additional vortices in the lock-in region, as explained by Govardhan and Williamson (2000), can be attributed to the phenomenon of vortex splitting,

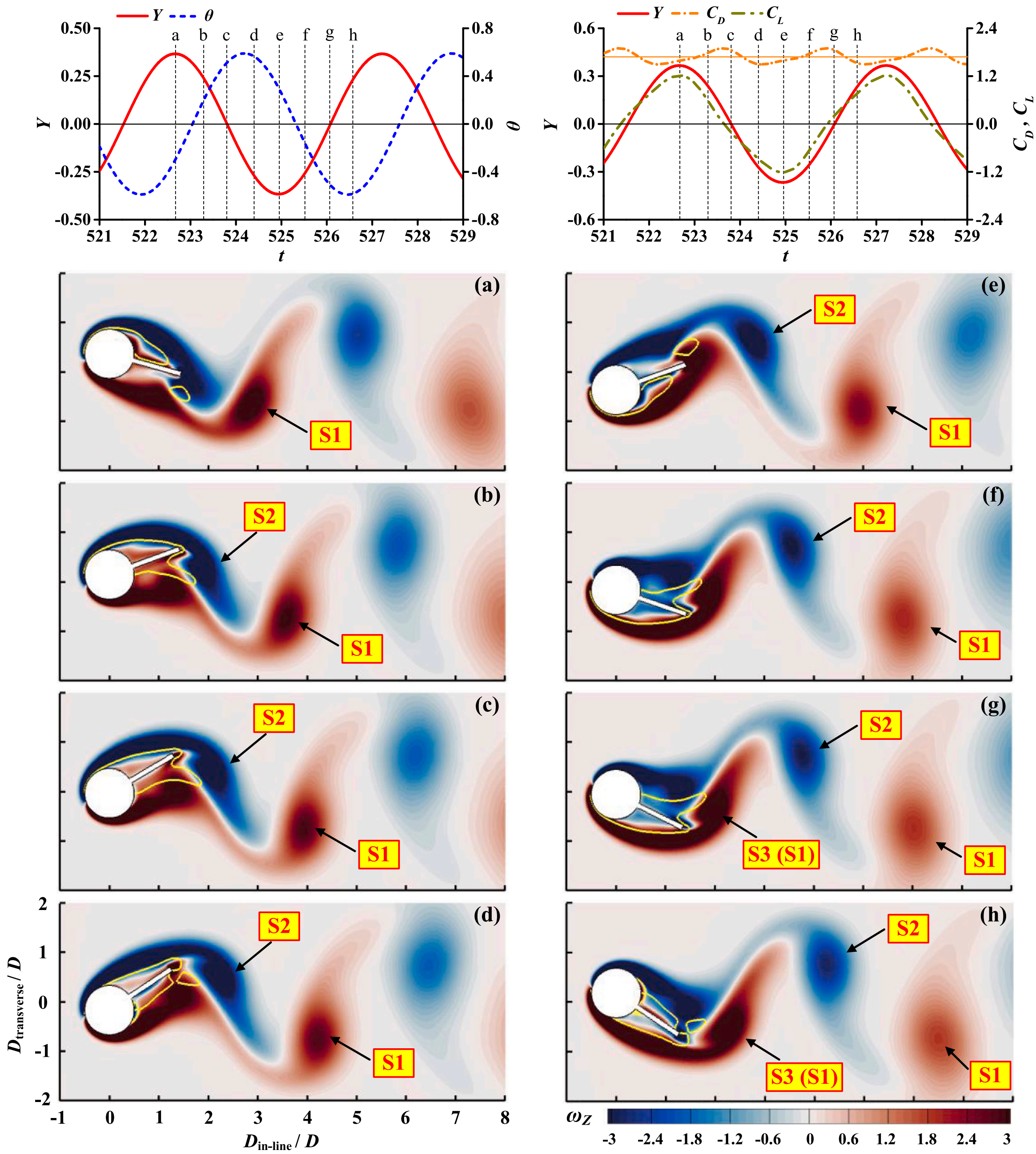

Fig. 17. Evolutions of 2S wake structures at $U_\theta = 5$ and $U_y = 5$ (non-bifurcation).

which is primarily generated by high-amplitude oscillations. Fig. 7 illustrates that, with an increase in U_θ (actually decreasing restoring forces in the rotational direction), both vibration and rotation amplitudes significantly increase and the lock-in region is broadened. Consequently, the 2T mode shown in Fig. 16 appears at relatively high U_θ values, with a wider associated control range.

To provide a comprehensive understanding of the interactions between wake modes and coupled movements, Figs. 17–22 depict the typical evolutions of 2S, 2P, 2S*, and 2T modes over one vibration period. Additionally, the same wake modes in both bifurcation and non-bifurcation region are compared to explain the underlying physics. Each figure presents the time histories of displacements, rotation angles, and hydrodynamic coefficients. The horizontal lines, either solid or dashed, represent the time-averaged values. Eight instantaneous instants within the vibration displacement curve are marked to capture key movements and vorticity fields. The yellow solid lines in vorticity snapshots represent the contour of $u = 0$.

Fig. 17 reveals a phase difference of approximately 90° between the displacement and rotation angle. From instant (a) to (d), the cylinder-plate body undergoes a downward motion while rotating in an anti-clockwise direction. During this period, the shear layer on the upper side of the cylinder-plate body reattaches to the tip of the plate, gradually forming an isolated vortex (S2). Meanwhile, the lower shear layer rolls up in the region below the splitter plate. At instant (e), as the cylinder-plate body starts rotating clockwise, the lower shear layer bypasses and is cut off by the plate tip, leading to the shedding of vortex S2. This shedding process repeats during the second half of the vibration period due to the non-bifurcation behavior. Consequently, the typical 2S vortex shedding mode is presented. Different from the 2S mode for the vibration-only case in Fig. 4 where shear layers directly skim over the cylinder-plate body, the reattachment behavior in Fig. 17 occurs more easily. This disparity suggests that flow-induced rotations play an

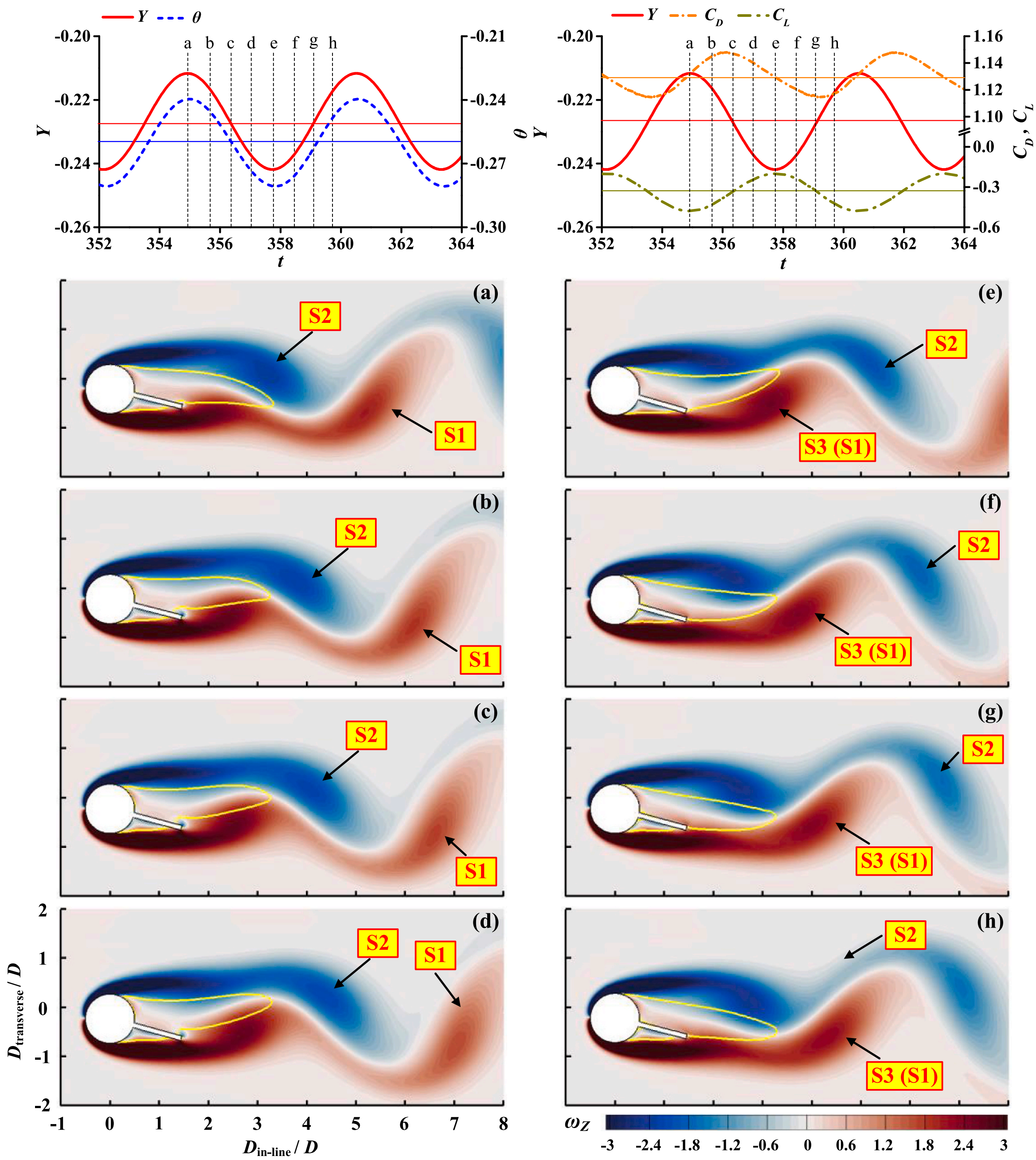

Fig. 18. Evolutions of 2S wake structures at $U_\theta = 18$ and $U_y = 18$ (bifurcation).

important role in enhancing fluid-structure interactions.

After the symmetry-breaking bifurcation, the wake flow and reattachment behavior exhibit notable differences compared to the case without bifurcation, despite both cases featuring the same vortex shedding mode. As seen in Fig. 18, the cylinder-plate body rotates in a clockwise direction and reaches a new equilibrium position, causing an asymmetric configuration relative to the flow direction. Due to the relatively small vibration and rotation amplitudes, the cylinder-plate body appears nearly stationary during the oscillation process. A noteworthy observation is that in the presence of the bifurcation, the lower shear layer consistently reattaches to the plate tip, while reattachment does not occur on the upper side of the cylinder-plate body. Consequently, vortices S1 and S2, characterized by different sizes, are shed from the upper surface of the cylinder and the plate tip, respectively. The contour line of $u = 0$ highlights the simplified reattachment behavior in the bifurcation region. Additionally, the recirculation region exhibits a significantly increased length compared to the non-bifurcation region, despite both regions presenting the 2S vortex shedding mode.

The 2S* vortex shedding mode observed in the lock-in region is similar with the 2S mode in Fig. 17. As shown in Fig. 19, following the shedding from the cylinder-plate body, the isolated vortex tends to split into two smaller vortices in the transverse direction. This splitting behavior is attributed to the relatively high-amplitude oscillations experienced by the system. As a result, the wake flows associated with the 2S* mode appear wider compared to those 2Smode in Fig. 17. However, it should be noted that the complete splitting process is not fully realized as the vortex continues to migrate downwards. Instead, only one core is observed in each vortex within the far wake field. This observation indicates that the 2S* vortex shedding mode arises as a combined result of the high-amplitude vibrations and the influence of viscous forces.

Figs. 20 and 21 present the evolutions of 2P vortex shedding mode in

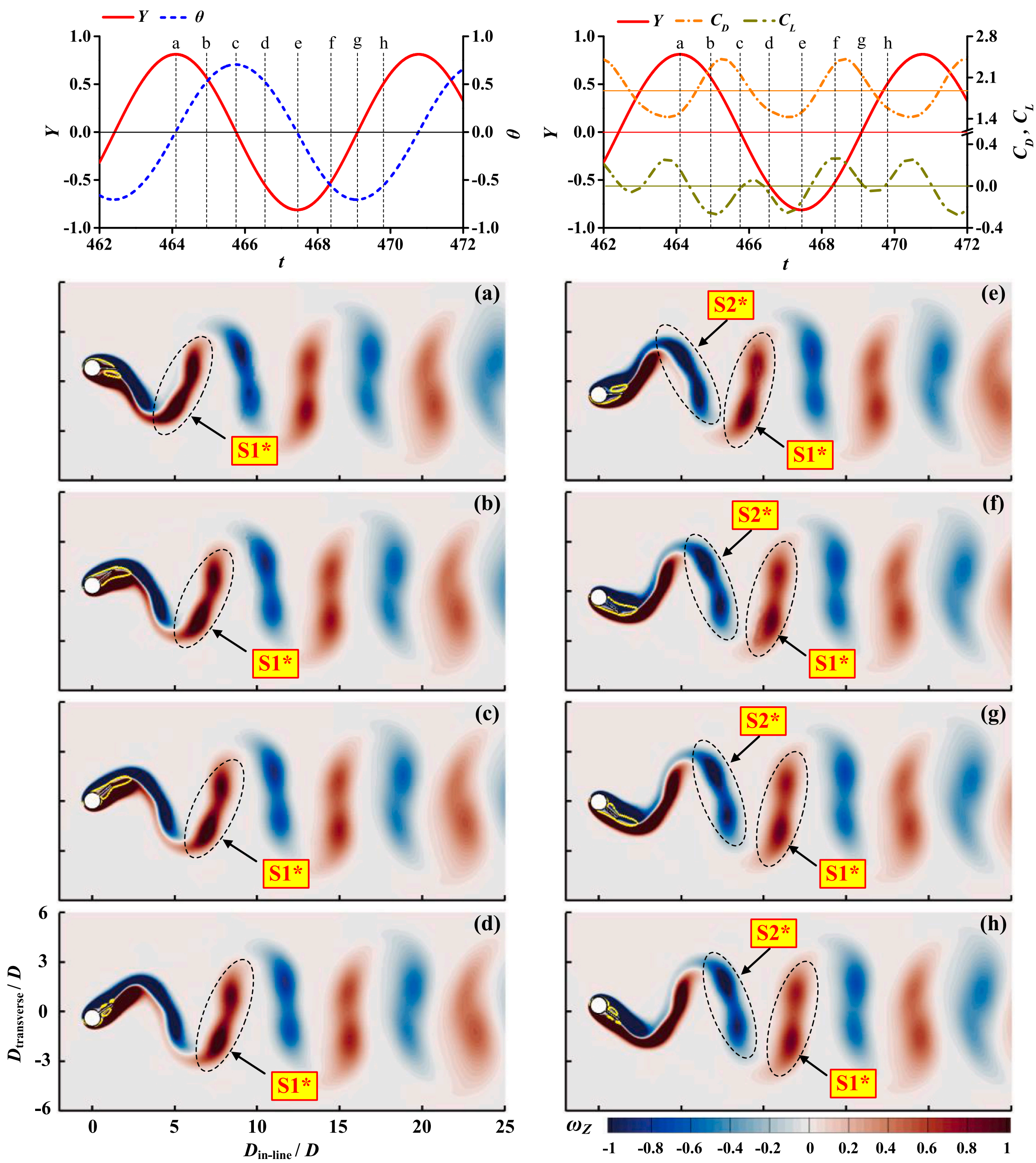

Fig. 19. Evolutions of 2S* wake structures at $U_\theta = 8$ and $U_y = 8$.

both non-bifurcation and bifurcation regions, respectively. The formation of 2P mode is associated with the stretching and splitting of each vortex (Govardhan and Williamson, 2000), which can be explained by the high-amplitude oscillations. Similar to the comparative results of the 2S mode in Figs. 17 and 18, the 2P mode in the non-bifurcation region, as depicted in Fig. 20, exhibits a symmetric configuration. In this case, two pairs of vortices are identical and shed alternately from the two sides of the cylinder-plate body. In contrast, the 2P mode in bifurcation region, as shown in Fig. 21, displays a significantly asymmetric profile relative to the oncoming flow. Due to negative deflections, the lower shear layers in Fig. 21 consistently reattach to the plate tip, while the upper shear layers originating from the cylinder surface undergo noticeable stretching and can roll up behind the cylinder-plate body. Consequently, the two vortices contained in P1 exhibit different sizes, with the smaller one dissipating quickly. On the other hand, those vortices in P2 posses comparable energy and size, resulting in slower dissipation. The distributions of the contour line of $u = 0$ indicate that the 2P mode in the bifurcation region exhibits simpler reattachment behavior and a longer recirculation region compared to the non-bifurcation region.

According to Williamson and Jauvtis (2004), the 2T vortex shedding mode comprises 2 triplets of vortices in each period. As shown in Fig. 22, we can observe a counter-rotating vortex pair, which is similar to the vortex pair in the 2P mode. Besides, a third principal vortex is generated, which might be attributed to the system dynamics associated with the 2T mode. During the downward migration, the three vortices in both T1 and T2 become different in size. One vortex remains clearly recognizable, while the other two vortices dissipate quickly. This dissipation process highlights the dynamic evolution and energy distribution within the 2T vortex shedding mode.

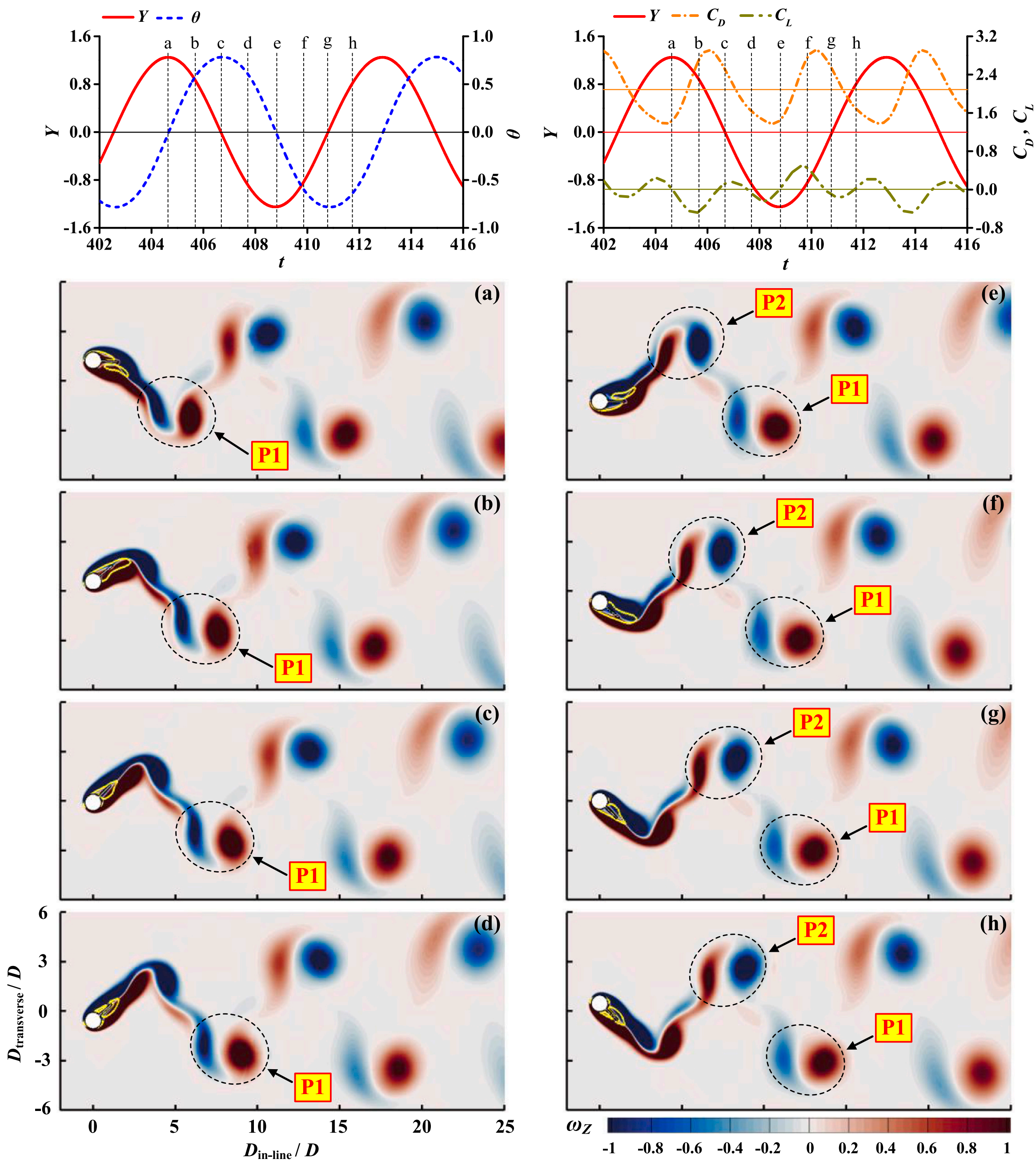

Fig. 20. Evolutions of 2P wake structures at $U_\theta = 12$ and $U_y = 10$ (non-bifurcation).

3.5. Applications in energy harvesting

The numerical results in Sec. 3.2 show that the passive rotations not only alter oscillation modes but also amplify the vibration amplitudes. This observation suggests the feasibility of employing passive rotations as a means to enhance the energy harvesting capability derived from flow-induced vibration. The vibrational and rotational output power can be calculated as:

$$P_y = \frac{1}{T}\int_0^T F_L \dot{y}\,\mathrm{d}t = \frac{1}{T}\int_0^T \left(m\ddot{y} + C_y\dot{y} + K_y y\right)\dot{y}\,\mathrm{d}t \tag{23}$$

$$P_\theta = \frac{1}{T}\int_0^T M_\theta \dot{\theta}\,\mathrm{d}t = \frac{1}{T}\int_0^T \left(I_\theta\ddot{\theta} + C_\theta\dot{\theta} + K_\theta\theta\right)\dot{\theta}\,\mathrm{d}t \tag{24}$$

where T is the vibration/rotation period. The nonzero term in Eqs. (23) and (24) on the right hand is the velocity term and thus the equations of output power can be simplified to:

$$P_y = \frac{1}{T}\int_0^T C_y \dot{y}^2 \mathrm{d}t \tag{25}$$

$$P_\theta = \frac{1}{T}\int_0^T C_\theta \dot{\theta}^2 \mathrm{d}t \tag{26}$$

The velocity term $\dot{y}$ and $\dot{\theta}$ can be obtained from time-histories of the displacement and rotation angle. Then the output power P_y and P_θ can be calculated by directly integrating $C_y\dot{y}^2$ and $C_\theta\dot{\theta}^2$ in one period.

Fig. 23 compares the vibrational, rotational, and total output

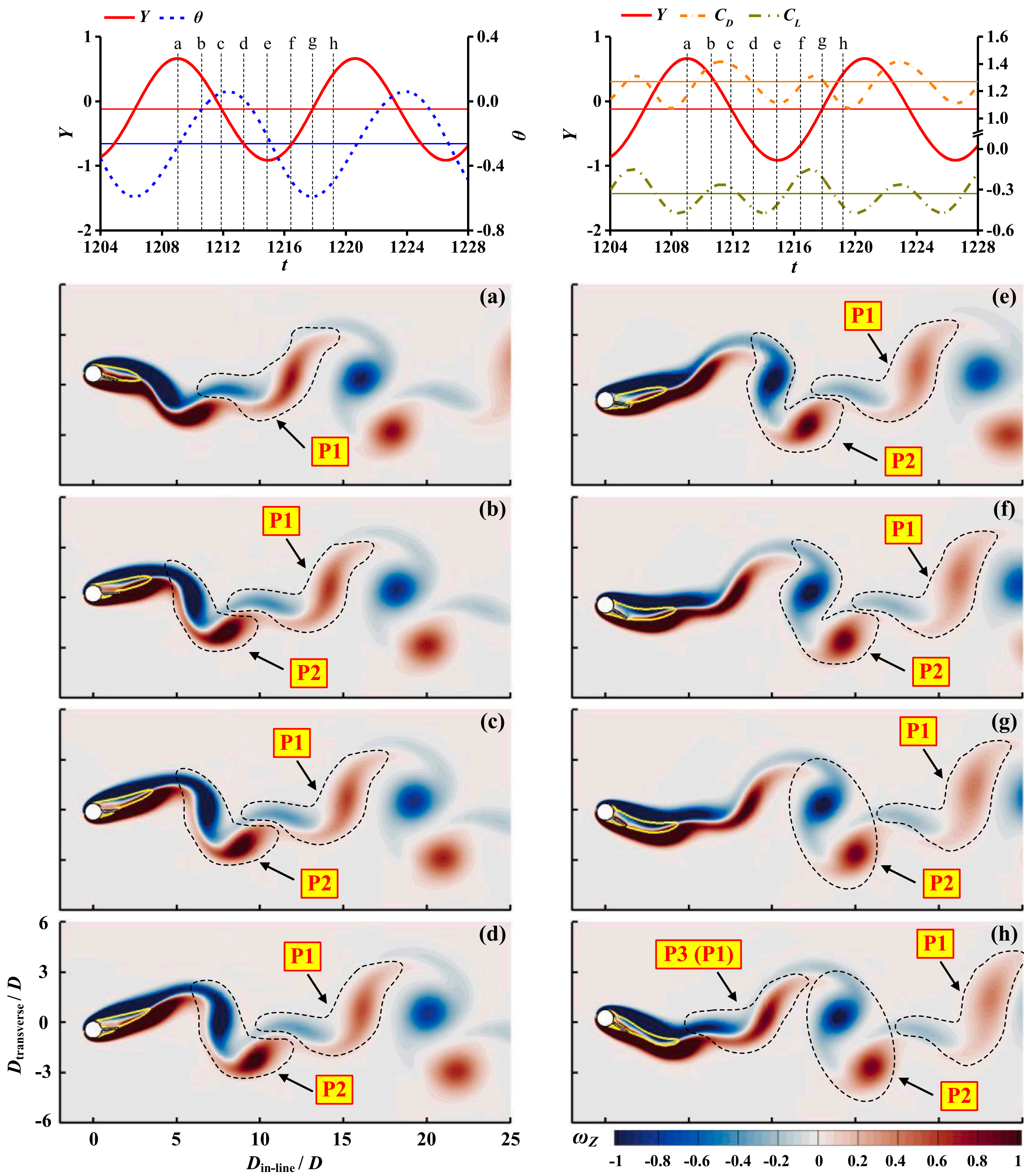

Fig. 21. Evolutions of 2P wake structures at $U_\theta = 18$ and $U_y = 14$ (bifurcation).

mechanical power under various rotational reduced velocities. The ratio of the vibrational power to total power is also plotted to illustrate the contributions. In Fig. 23(a), the power remains minimal throughout the whole U_y range, despite the galloping responses with increasing amplitudes in U_y = 7–18 (Fig. 4). However, when passive rotations are considered, substantial enhancements in vibrational power are observed, particularly in terms of peak power and the extent of the control region. Generally, the larger U_θ values correspond to the higher peak power and the broader control region. The maximum output power $P_y = 1.73$ μW is achieved at $U_\theta = 18$ and $U_y = 8$. Fig. 22(b) demonstrates that the variations of rotational power (P_θ) follow a similar trend to those of vibrational power (P_y), albeit with significantly smaller values (less than 0.025 μW). Consequently, the total power curves in Fig. 23(c) closely align with the vibrational power curves. Furthermore, the ratio of P_y/P_{total} in Fig. 23(d) exceed 80% in most cases. To summarize, although the passive rotations do not contribute significantly to the total output power, they play a vital role in enhancing flow-induced vibrations, leading to a substantial increase in vibrational power.

Since the rotational energy is considerably small in this work, we mainly consider the power extraction in terms of the flow-induced vibration along transverse direction. The energy of the oscillating cylinder-plate body is originally extracted from the kinetic energy of the flow for the projected area of the cylinder, which can be given as:

$$P_{fluid} = \frac{1}{2}\rho U^3 (D + D_m) \tag{27}$$

where D_m is the distance between the maximum positive and negative displacement. Thus, the energy transfer ratio (or power extraction efficiency, λ) for the flow-induced vibration can be written as:

$$\lambda = \frac{P_y}{P_{fluid} \times Betz\ Limit} \times 100\% \tag{28}$$

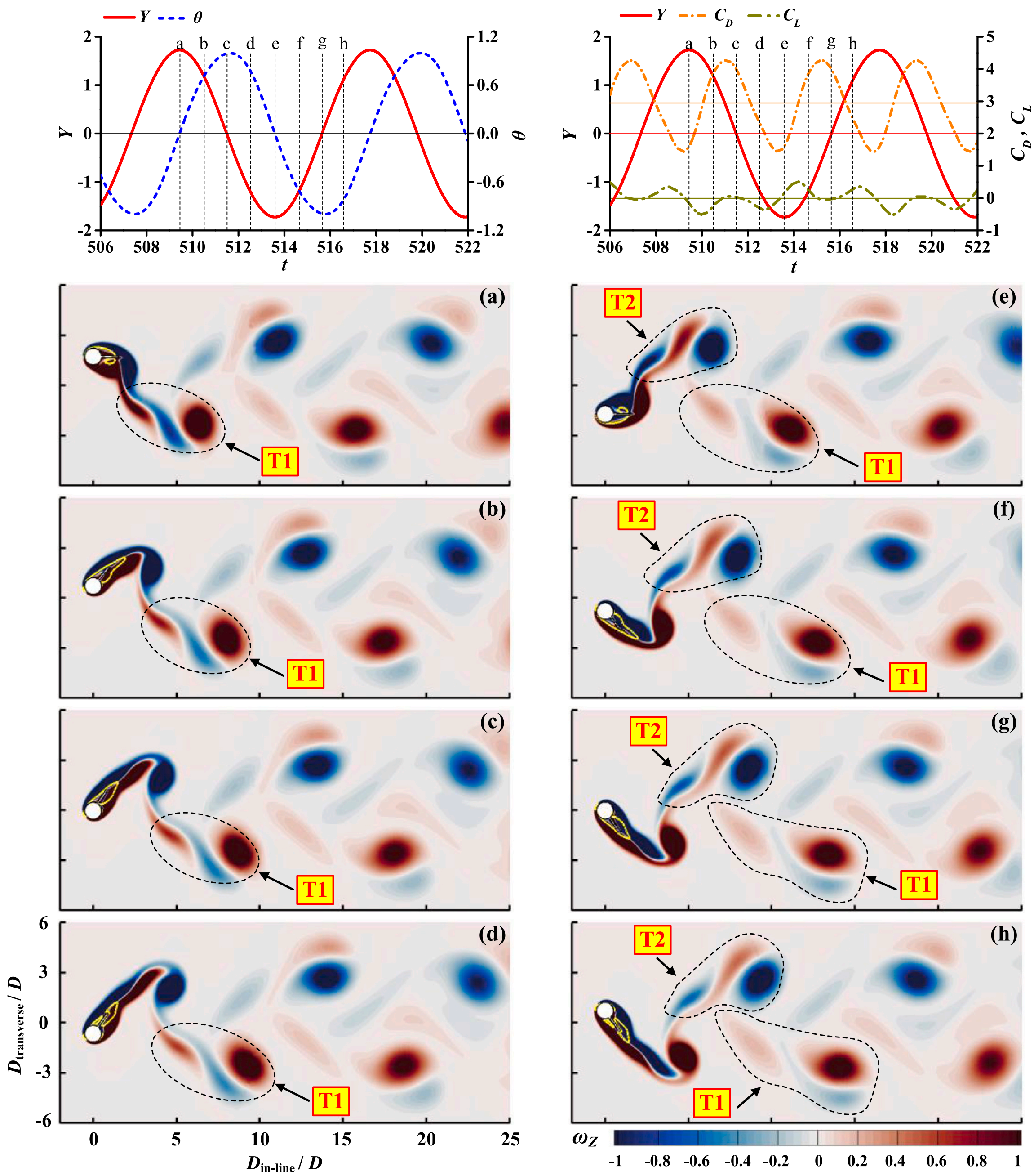

Fig. 22. Evolutions of 2T wake structures at $U_\theta = 18$ and $U_y = 10$.

where Betz Limit (=16/27) is the theoretical maximum power that can be extracted from an open flow (Sun et al., 2017).

Fig. 24 reports the vibration energy transfer ratio for the vibration-only case and four coupled cases. Basically, the energy transfer ratio follows a similar trend as the output power in Fig. 23(a). For the vibration-only case, the energy transfer ratio is sufficiently small with no more than 0.5%, even though in the large U_y range where galloping-type oscillations are observed. In contrast, the transfer ratio becomes significantly large in the lock-in region when passive rotations are considered. The maximum ratio of $\lambda = 3.501\%$ is obtained at $U_\theta = 18$ and $U_y = 8$. Generally, passive rotations lead to an increased vibration energy transfer ratio within a relatively small reduced velocity range. This makes it a suitable and preferred method for the applications in energy harvesting from flow-induced vibrations.

4. Conclusions

Vibration and rotation are two typical fluid-structure interaction motions. These motions can manifest individually or simultaneously. The individual vibration/rotation cases have been extensively studied while the coupled cases are less reported. Nevertheless, it is important to acknowledge that coupled responses, such as those observed in falling leaves and offshore wind turbines, are more prevalent in both natural phenomena and engineering applications. Consequently, investigating the coupled dynamics of flow-induced vibration and rotation holds greater significance from both academic and practical perspectives. In this work, to investigate the coupled responses of flow-induced vibration and rotation for an elastically mounted cylinder-plate body, numerical simulations are conducted in a wide vibrational reduced velocity range of $U_y = 3$–18 under four rotational reduced velocities ($U_\theta = 5$, 8, 12, and 18) at a low Reynolds number of 120. The main conclusions are as

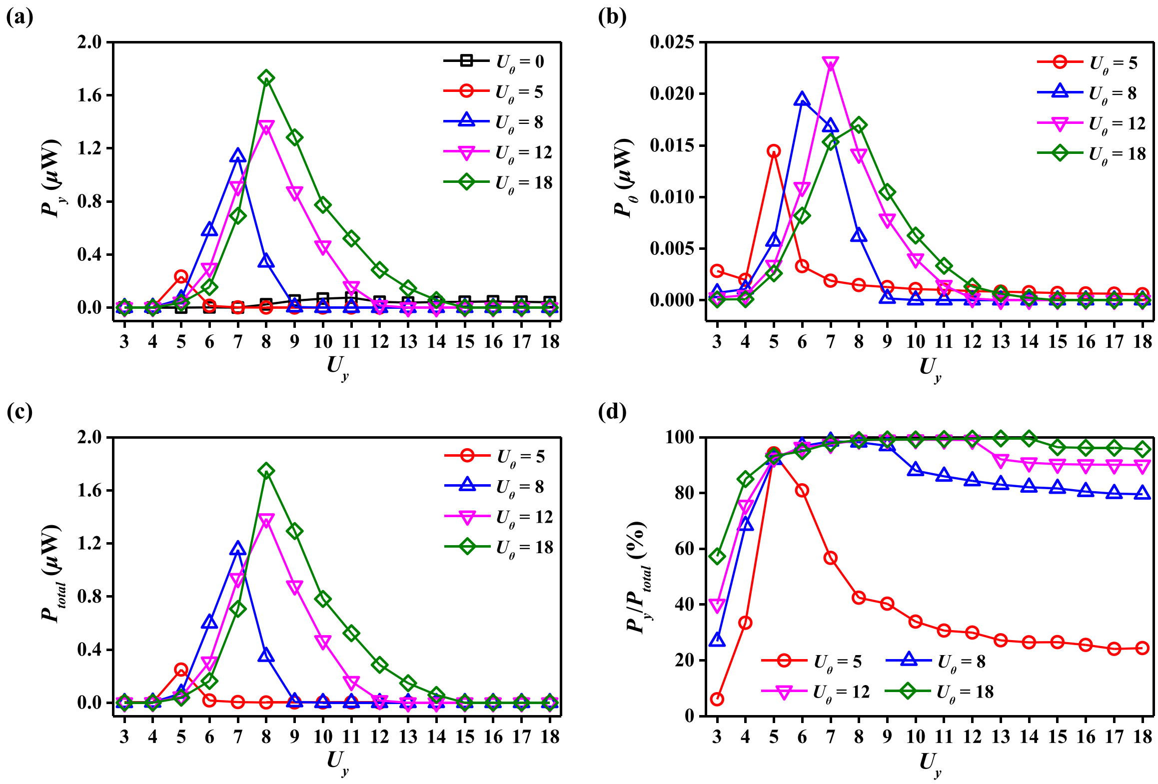

Fig. 23. Output mechanical power: (a) vibration; (b) rotation; (c) the total; (d) ratio of the vibrational part to the total.

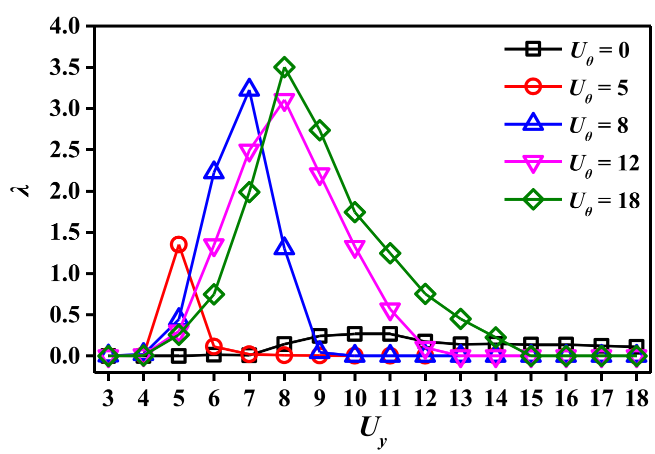

Fig. 24. Comparisons of vibration energy transfer ratio (or power extraction efficiency).

follows:

(1) For the vibration-only case, the full interaction between VIV and galloping is identified and the boundary is located in $U_y = 6$–7. The 2S and 2P vortex shedding mode are observed in the VIV and galloping region, respectively. For the rotation-only case, the bifurcation occurs when $U_\theta > 12$, where the cylinder-plate body rotates about a non-zero equilibrium position. The VIV-like rotational pattern and 2S vortex shedding mode are recognized in the whole range of $U_\theta = 3$–18.

(2) According to the appearance of bifurcation, the coupled responses can be classified into three types: non-bifurcation responses (in most cases), bifurcation only in rotation responses ($U_y = 3$–4 for $U_\theta = 18$), and bifurcation in both vibration and rotation responses ($U_y = 11$ for $U_\theta = 12$, $U_y = 11$–18 for $U_\theta = 18$). The passive rotations not only alter the vibration modes but also amplify the amplitudes and broad the lock-in region. Unlike the full interaction between VIV and galloping for the vibration-only case, typical VIV modes including the initial branch (IB), lock-in, and desynchronization branch (DB) are recognized for $U_\theta = 8$, 12, and 18. However, a clearly defined lock-in region is not observed for $U_\theta = 5$. As U_θ increases, the peak vibration amplitudes increase, the onset U_y of the lock-in region becomes larger, and the lock-in region becomes wider. The flow-induced rotation responses are affected by vibrations, and the larger the U_θ, the wider the affected regions.

(3) In the coupled cases, the phase differences between displacements and lift coefficients undergo a significant jump from 0° to 180° within the lock-in region. This jump is accompanied by a transition in the added mass coefficients from positive to negative values. The U_y range exhibiting this phase jump increases with larger U_θ values. Phase differences between displacements and rotation angles reveal different dynamic responses. The achievement in streamlined profile, where the projected area is no larger than the diameter of the circular cylinder, is determined by two conditions. One is when the vibration and rotation amplitudes are substantially small and another is when the phase between displacements and rotation angles is close to 90°. Non-streamlined profiles are observed when the oscillations approach the lock-in region from the initial branch.

(4) The vortex shedding modes of the coupled responses are strongly related to the flow-induced oscillation modes. The 2S mode is predominated in the IB and DB region, while the 2P, 2S*, and 2T modes appear in lock-in region. When bifurcation occurs, the reattachment behavior on the splitter plate becomes simpler compared to the non-bifurcation region. Additionally, the length of the recirculation region is significantly increased.

(5) Passive rotations can enhance the flow-induced vibrations and consequently lead to the increased vibrational power and energy transfer ratio, although the they do not contribute significantly to the total output power. The peak power and energy transfer ratio for the coupled responses appear in the lock-in region.

Although some useful conclusions are obtained based on the present study, limitations in this work can be noted. Firstly, the two-dimensional simulations are conducted at a specific low Reynolds number of 120, which is significantly different from the three-dimensional conditions. Secondly, only one specific cylinder-plate body ($L^* = 1$ and $G^* = 0$) is employed. Finally, only four rotational reduced velocities are considered. Therefore, further extensive investigations are needed, for example, to study a range of Reynolds number to cover three-dimensional effects and verify system's energy harvesting capacity. In order to optimize the energy harnessing, studies can be extended to include a wider range of structural parameters such as the plate length and the distance between the cylinder and plate. More importantly, investigations of the effects of FIV on FIR responses should be conducted to provide a relatively comprehensive guidance on the coupled responses.

CRediT authorship contribution statement

Tao Tang: Investigation, Formal analysis, Writing – original draft. **Hongjun Zhu:** Conceptualization, Methodology, Resources, Supervision, Writing – review & editing. **Qing Xiao:** Supervision, Writing – review & editing. **Quanyu Chen:** Investigation, Formal analysis. **Jiawen Zhong:** Formal analysis. **Yingmei Li:** Formal analysis. **Tongming Zhou:** Writing – review & editing.

Declaration of competing interest

The authors declare that they have no known competing financial interests or personal relationships that could have appeared to influence the work reported in this paper.

Data availability

Data will be made available on request.

Acknowledgments

This research was supported by the National Natural Science Foundation of China (Grant No. 51979238), Sichuan Science and Technology Program (No. 2023NSFSC1953), and China Scholarship Council. The work was carried out in the computer cluster of the laboratory of offshore oil and gas engineering at Southwest Petroleum University (SWPU).

References

Apelt, C.J., West, G.S., 1975. The effects of wake splitter plates on bluff-body flow in the range of $10^4 < Re < 5\times10^4$. part 2. J. Fluid Mech. 71, 145–160.
Apelt, C.J., West, G.S., Szewczyk, A.A., 1973. The effects of wake splitter plates on the flow past a circular cylinder in the range of $10^4 < Re < 10^5$. J. Fluid Mech. 61, 187–198.
Assi, G.R.S., Bearman, P.W., 2015. Transverse galloping of circular cylinders fitted with solid and slotted splitter plates. J. Fluid Struct. 54, 263–280.
Assi, G.R.S., Bearman, P.W., Tognarelli, M.A., 2014. On the stability of a free-to-rotate short-tail fairing and a splitter plate as suppressors of vortex-induced vibration. Ocean Eng. 92, 234–244.
Assi, G.R.S., Bearman, P.W., Kitney, N., 2009. Low drag solutions for suppressing vortex-induced vibration of circular cylinders. J. Fluid Struct. 25, 666–675.
Bearman, P.W., Gartshore, I.S., Maull, D.J., Parkinson, G.V., 1987. Experiments on flow-induced vibration of a square-section cylinder. J. Fluid Struct. 1, 19–34.
Bernitsas, M.M., Raghavan, K., Ben-Simon, Y., Garcia, E.M.H., 2008. VIVACE (vortex-induced vibration aquatic clean energy): a new concept in generation of clean and renewable energy from fluid flow. J. Offshore Mech. Arctic Eng. 130, 041101.
Bhatt, R., Alam, M.M., 2018. Vibrations of a square cylinder submerged in a wake. J. Fluid Mech. 853, 301–332.
Carmo, B.S., Meneghini, J.R., 2006. Numerical investigation of the flow around two circular cylinders in tandem. J. Fluid Struct. 22, 979–988.
Chen, W.L., Ji, C.N., Xu, D., Zhang, Z.M., Wei, Y.H., 2020. Flow-induced vibrations of an equilateral triangular prism at various angles of attack. J. Fluid Struct. 97, 103099.
Choi, H., Jeon, W.P., Kim, J.S., 2008. Control of flow over a bluff body. Annu. Rev. Fluid Mech. 40, 113–139.
Cimbala, J.M., Chen, K.T., 1994. Supercritical Reynolds number experiments on a freely rotatable cylinder/splitter plate body. Phys. Fluids 6, 2440.
Cimbala, J.M., Garg, S., 1991. Flow in the wake of a freely rotatable cylinder with splitter plate. AIAA J. 29, 1001–1003.
Govardhan, R., Williamson, C.H.K., 2000. Modes of vortex formation and frequency response of a freely vibrating cylinder. J. Fluid Mech. 420, 85–130.
Gsell, S., Bourguet, R., Braza, M., 2016. Two-degree-of-freedom vortex-induced vibrations of a circular cylinder at Re = 3900. J. Fluid Struct. 67, 156–172.
Gu, F., Wang, J.S., Qiao, X.Q., Huang, Z., 2012. Pressure distribution, fluctuating forces and vortex shedding behavior of circular cylinder with rotatable splitter plates. J. Fluid Struct. 28, 263–278.
Henderson, R.D., 1997. Nonlinear dynamics and pattern formation in turbulent wake transition. J. Fluid Mech. 3352, 65.
Hu, Z.M., Wang, J.S., Sun, Y.K., Zheng, H.X., 2021. Flow-induced vibration suppression for a single cylinder and one-fixed-one-free tandem cylinders with double tail splitter plates. J. Fluid Struct. 106, 103373.
Huang, R.F., Hsu, C.M., Chen, Y.T., 2017. Modulating flow and aerodynamic characteristics of a square cylinder in crossflow using a rear jet injection. Phys. Fluids 29, 015103.
Hwang, J.Y., Yang, K.S., Sun, S.H., 2003. Reduction of flow-induced forces on a circular cylinder using a detached splitter plate. Phys. Fluids 15, 2433.
Kawai, H., 1990. Discrete vortex simulation for flow around a circular cylinder with a splitter plate. J. Wind Eng. Ind. Aerod. 33, 153–160.
Kwon, K., Choi, H., 1996. Control of laminar vortex shedding behind a circular cylinder using splitter plate. Phys. Fluids 8, 479.
Liang, S.P., Wang, J.S., Hu, Z.M., 2018. VIV and galloping response of a circular cylinder with rigid detached splitter plates. Ocean Eng. 162, 176–186.
Lu, L., Guo, X.L., Tang, G.Q., Liu, M.M., Chen, C.Q., Xie, Z.H., 2016. Numerical investigation of flow-induced rotary oscillation of circular cylinder with rigid splitter plate. Phys. Fluids 28, 093604.
Mannini, C., Marra, A.M., Bartoli, G., 2014. VIV-galloping instability of rectangular cylinders: review and experiments. J. Wind Eng. Ind. Aerod. 132, 109–124.
Mannini, C., Marra, A.M., Massai, T., Bartoli, G., 2016. Interference of vortex-induced vibration and transverse galloping for a rectangular cylinder. J. Fluid Struct. 66, 403–423.
Miyata, T., Miyazaki, M., Yamada, H., 1983. Pressure distribution measurements for wing induced vibrations of box girder bridges. J. Wind Eng. Ind. Aerod. 14, 223–234.
Ozkan, G.M., Firat, E., Akilli, H., Norberg, C., 2017. Passive flow control in the near wake of a circular cylinder using attached permeable and inclined short plates. Ocean Eng. 134, 35–49.
Ozone, S., 1999. Flow control of vortex shedding by a short splitter plate asymmetrically arranged downstream of a cylinder. Phys. Fluids 11, 2928–2934.
Qiu, Y., Sun, Y., Wu, Y., Tamura, Y., 2014. Effects of splitter plates and Reynolds number on the aerodynamic loads acting on a circular cylinder. J. Wind Eng. Ind. Aerod. 127, 40–50.
Rashidi, S., Hayatdavoodi, M., Esfahani, J.A., 2016. Vortex shedding suppression and wake control: a review. Ocean Eng. 126, 57–80.
Robertson, I., Li, L., Sherwin, S.J., Bearman, P.W., 2003. A numerical study of rotational and transverse galloping rectangular bodies. J. Fluid Struct. 17, 681–699.
Rostami, A.B., Armandei, M., 2017. Renewable energy harvesting by vortex-induced vibrations: review and benchmarking of technologies. Renew. Sustain. Energy Rev. 70, 193–214.
Sahu, T.R., Furquan, M., Jaiswal, Y., Mittal, S., 2019. Flow-induced vibration of a circular cylinder with rigid splitter plate. J. Fluid Struct. 89, 244–256.
Serson, D., Meneghini, J.R., Carmo, B.S., Volpe, E.V., Gioria, R.S., 2014. Wake transition in the flow around a circular cylinder with a splitter plate. J. Fluid Mech. 755, 582–602.
Song, J., Hu, G., Tse, K.T., Li, S.W., Kwok, K.C.S., 2017. Performance of a circular cylinder piezoelectric wind energy harvester fitted with a splitter plate. Appl. Phys. Lett. 111, 223903.
Stappenbelt, B., 2010. Splitter-plate wake stabilisation and low aspect ratio cylinder flow-induced vibration mitigation. Int. J. Offshore Polar Eng. 20, 1–6.
Sun, H., Ma, C.H., Kim, E.S., Nowakowski, G., Mauer, E., Bernitsas, M.M., 2017. Hydrokinetic energy conversion by two rough tandem-cylinders in flow induced motions: effect of spacing and stiffness. Renew. Energy 107, 61–80.
Sun, X., Suh, C.S., Ye, Z.H., Yu, B., 2020. Dynamics of a circular cylinder with an attached splitter plate in laminar flow: a transition from vortex-induced vibration to galloping. Phys. Fluids 32, 027104.
Sun, Y.K., Wang, J.S., Fan, D.X., Zheng, H.X., Hu, Z.M., 2022. The roles of rigid splitter plates in flow-induced vibration of a circular cylinder. Phys. Fluids 34, 114114.
Tang, T., Zhu, H.J., Chen, Q.Y., Li, G.M., Zhou, T.M., 2022a. CFD analysis of flow-induced rotation of a circular cylinder with a detached rear splitter plate in laminar flow. Ocean Eng. 266, 112703.
Tang, T., Zhu, H.J., Chen, Q.Y., Zhong, J.W., Gao, Y., 2023a. Dynamic response of a circular cylinder in the presence of a detached splitter plate: on the gap distance sensitivity. J. Fluid Struct. 119, 103888.

Tang, T., Zhu, H.J., Li, G.M., Song, J.Z., 2023b. Comparative study of the flow-induced vibration of a circular cylinder attached with front and/or rear splitter plates at a low Reynolds number of 120. J. Offshore Mech. Arctic Eng. 145, 011903.
Tang, T., Zhu, H.J., Wang, J.S., Alam, M.M., Song, J.Z., Chen, Q.Y., 2022b. Flow-induced rotation modes and wake characteristics of a circular cylinder attached with a splitter plate at low Reynolds numbers. Ocean Eng. 266, 112823.
Wang, J.L., Geng, L.F., Ding, L., Zhu, H.J., Yurchenko, D., 2020. The state-of-the-art review on energy harvesting from flow-induced vibrations. Appl. Energy 267, 114902.
Williamson, C.H.K., Jauvtis, N., 2004. A high-amplitude 2T mode of vortex-induced vibration for a light body in XY motion. Eur. J. Mech. B Fluid 23, 107–114.
Xie, F.F., Deng, J., Xiao, Q., Zheng, Y., 2012. A numerical simulation of VIV on a flexible circular cylinder. Fluid Dynam. Res. 44, 045508.
Xu, J.C., Sen, M., Gad-el-Hak, M., 1990. Low-Reynolds number flow over a rotatable cylinder-splitter plate body. Phys. Fluids 2, 1925–1927.
Xu, J.C., Sen, M., Gad-el-Hak, M., 1993. Dynamics of a rotatable cylinder with splitter plate in uniform flow. J. Fluid Struct. 7, 401–416.
Zdravkovich, M.M., 1981. Review and classification of various aerodynamic and hydrodynamic means for suppressing vortex shedding. J. Wind Eng. Ind. Aerod. 7, 145–189.
Zhang, M.J., Wang, X., Øiseth, O., 2021. Torsional vibration of a circular cylinder with an attached splitter plate in laminar flow. Ocean Eng. 236, 109514.
Zhao, J.S., Leontini, J.S., Jacono, D.L., Sheridan, J., 2014. Fluid-structure interaction of a square cylinder at different angles of attack. J. Fluid Mech. 747, 688–721.
Zhao, M., 2013. Flow induced vibration of two rigidly coupled circular cylinders in tandem and side-by-side arrangements at a low Reynolds number of 150. Phys. Fluids 25, 123601.
Zhu, H.J., Li, G.M., Wang, J.L., 2020a. Flow-induced vibration of a circular cylinder with splitter plates placed upstream and downstream individually and simultaneously. Appl. Ocean Res. 97, 102084.
Zhu, H.J., Tang, T., Alam, M.M., Song, J.Z., Zhou, T.M., 2022. Flow-induced rotation of a circular cylinder with a detached splitter plate and its bifurcation behaviour. Appl. Ocean Res. 122, 103150.
Zhu, H.J., Tang, T., Gao, Y., Zhou, T.M., Wang, J.L., 2021a. Flow-induced vibration of a trapezoidal cylinder placed at typical flow orientations. J. Fluid Struct. 103, 103291.
Zhu, H.J., Tang, T., Wang, J.L., 2020b. Modification of wake flow and air-bubble-vortex interference in the flow control of a circular cylinder with a pair of air jets: effect of injection velocity. Ocean Eng. 214, 107766.
Zhu, H.J., Tang, T., Yang, H.H., Wang, J.L., Song, J.Z., Peng, G., 2021b. The state-of-the-art brief review on piezoelectric energy harvesting from flow-induced vibration. Shock Vib., 8861821
Zhu, H.J., Tang, T., Zhao, H.L., Gao, Y., 2019. Control of vortex-induced vibration of a circular cylinder using a pair of air jets at low Reynolds number. Phys. Fluids 31, 043603.
Zhu, H.J., Zhao, Y., Zhou, T.M., 2018. CFD analysis of energy harvesting from flow induced vibration of a circular cylinder with an attached free-to-rotate pentagram impeller. Appl. Energy 212, 304–321.